Front. Phys. 12(1), 127301 (2017)
DOI 10.1007/s11467-016-0605-2

REVIEW ARTICLE

Electron microscopy methods for space-, energy-, and time-resolved plasmonics

Arthur Losquin[1,*], **Tom T. A. Lummen**[2,†]

[1] *Department of Physics, Lund University, P.O. Box 118, SE-221 00 Lund, Sweden*
[2] *Laboratory for Ultrafast Microscopy and Electron Scattering, ICMP, École Polytechnique Fédérale de Lausanne, Station 6, CH-1015 Lausanne, Switzerland*
*E-mail: *arthur.losquin@fysik.lth.se, †tom.lummen@epfl.ch*
Received May 23, 2016; accepted June 24, 2016

Nanoscale plasmonic systems combine the advantages of optical frequencies with those of small spatial scales, circumventing the limitations of conventional photonic systems by exploiting the strong field confinement of surface plasmons. As a result of this miniaturization to the nanoscale, electron microscopy techniques are the natural investigative methods of choice. Recent years have seen the development of a number of electron microscopy techniques that combine the use of electrons and photons to enable unprecedented views of surface plasmons in terms of combined spatial, energy, and time resolution. This review aims to provide a comparative survey of these different approaches from an experimental viewpoint by outlining their respective experimental domains of suitability and highlighting their complementary strengths and limitations as applied to plasmonics in particular.

Keywords plasmonics, electron microscopy, Electron Energy Loss Spectroscopy (EELS), cathodoluminescence, Photoemission Electron Microscopy (PEEM), Photo-Induced Near-field Electron Microscopy (PINEM), Electron Energy Gain Spectroscopy (EEGS)

PACS numbers 73.20.Mf, 36.40.Gk, 07.78.+s, 29.30.Dn, 68.37.-d

Contents

1 Introduction

The field of plasmonics and metamaterials is strongly driven by its potential technological applications, as surface plasmons are envisioned as the information carriers in next-generation devices. This is mainly because of their potential to bridge the size-compatibility gap between state-of-the-art nanoelectronics and photonics [1, 2]. Much of the field of plasmonics, which offers the ability to confine electromagnetic energy to subwavelength spatial scales as one of its principal advantages, is devoted to managing and guiding plasmons in structured nanoscale systems and improving field enhancement on the nanoscale. As a result, the spatial resolution of the

*Special Topic: Frontiers of Plasmonics (Ed. Hong-Xing Xu).

Frontiers of Physics

investigative techniques employed is crucial, and electron microscopy methods form the mainstay of plasmonics studies. Most often, the spatial characterization thus obtained is supplemented by measurements performed using optical techniques [3] such as (surface- or tip-enhanced) Raman microscopy [4–7] and scanning near-field optical microscopy (SNOM) [8–11]. Despite the limited spatial resolution of such optical methods, this combination of independent electron microscopy characterization and optical measurements has led to a tremendous amount of progress in the understanding of the field.

To properly resolve the full plasmonic picture, however, one would ideally require an adequate experimental resolution in all three domains, viz. space, energy, and time. Considering the typical experimental ranges of interest, this corresponds to having a spatial resolution on the subnanometer to few-nanometer scale, an energy resolution in the millielectron volt range, and an attosecond to picosecond time resolution. The need for such a challenging combined resolution is illustrated in Fig. 1, which shows a finite-difference time-domain (FDTD) simulation of the spectral and temporal response of a gold nanowire antenna. In this idealized model, a nanowire antenna is excited by a point dipole source radiating a broadband single-cycle electromagnetic pulse with its electric field oriented along the wire long axis [Figs. 1(a) and (b)]. This excitation pulse induces a traveling plasmonic wave packet in the nanoantenna, the corresponding spectral and spatial distributions of which are depicted in Fig. 1(c). Here, the signs in the plot represent the relative phases of the intensity antinodes of the clearly distinguishable resonant eigenmodes that are excited. Figure 1(d) illustrates several spectral intensity profiles along the wire axis (calculated from the Fourier components $|E_z(\omega)|^2$), which show that the plasmonic resonances occur in a broad spectral range of around 2 eV and have a natural full width at half-maximum (FWHM) of ∼120 meV. This sets the ideal energy resolution requirement from the infrared to the ultraviolet (UV) regime in the sub-100 meV range. Figure 1(e) shows the associated back-and-forth propagation of the wave packet in the nanowire in the time domain, which occurs on a few-femtosecond timescale. Figure 1(f) represents the dynamics of the plasmonic near-field energy confined to the wire (calculated from the E_z field envelope), which dissipates with an exponential time constant of ∼12 fs [see also Fig. 1(e)]. Depending on whether one wants to resolve plasmonic field oscillations, plasmon decay processes, or plasmon propagation, one thus requires a subfemtosecond to picosecond time resolution. Overall, considering that each of the relevant dimensional scales is at the current frontier of experimental science, the direct probing of plasmons in space, energy, and time presents a formidable experimental challenge. Nevertheless, a number of electron microscopy techniques have emerged in recent years to meet this challenge and explore the corresponding experimental void in plasmonics.

This review presents an overview of the ensemble of these techniques. By describing the underlying physical mechanisms of each method in turn, and highlighting their individual strengths and limitations, this review intends to convey an intuitive understanding of their applicability to measurements in plasmonics. Moreover, owing to the adopted modular layout, each of the individual methodology sections in Section 2 may also serve as a stand-alone introductory overview of the corresponding technique in terms of plasmonics. To maintain accessibility, we take a descriptive rather than an exhaustive approach throughout the review and refer the interested reader to more in-depth resources where appropriate.

2 Electron-based techniques for plasmonics

2.1 Overview

Before reviewing each of the relevant electron-based techniques in turn, it is useful to first place them in a general perspective by considering the underlying elementary mechanisms. We start with those techniques that use the microscope's electron beam itself to induce plasmonic excitations through the mechanism sketched in Fig. 2(a). In its most elementary description, an incident fast electron excites a surface plasmon in the specimen, losing energy in the process. The details of such electron energy loss (EEL) events can be retrieved through spectral analysis of the transmitted electrons; this procedure forms the basis of electron energy loss spectroscopy (EELS). After electron excitation, the plasmon can be dissipated either nonradiatively (through energy absorption in the specimen) or radiatively. In the latter case [Fig. 2(b)], the specimen emits a photon carrying information about the plasmon, which can be captured and spectrally analyzed using a cathodoluminescence (CL) detection system. EELS and CL were the first electron microscopy techniques employed to study plasmonics; consequently, they are presently the most widespread and well-understood. As they yield very similar information, they are discussed together in Section 2.2.

Although EELS and CL are highly suitable for obtaining information about the plasmon modes of a system, the electronic excitation used by these techniques (i) does not directly reflect how the sample responds to light excitation and (ii) limits the dynamical information that can be obtained. As a consequence, new approaches that employ in-microscope optical excitation in-

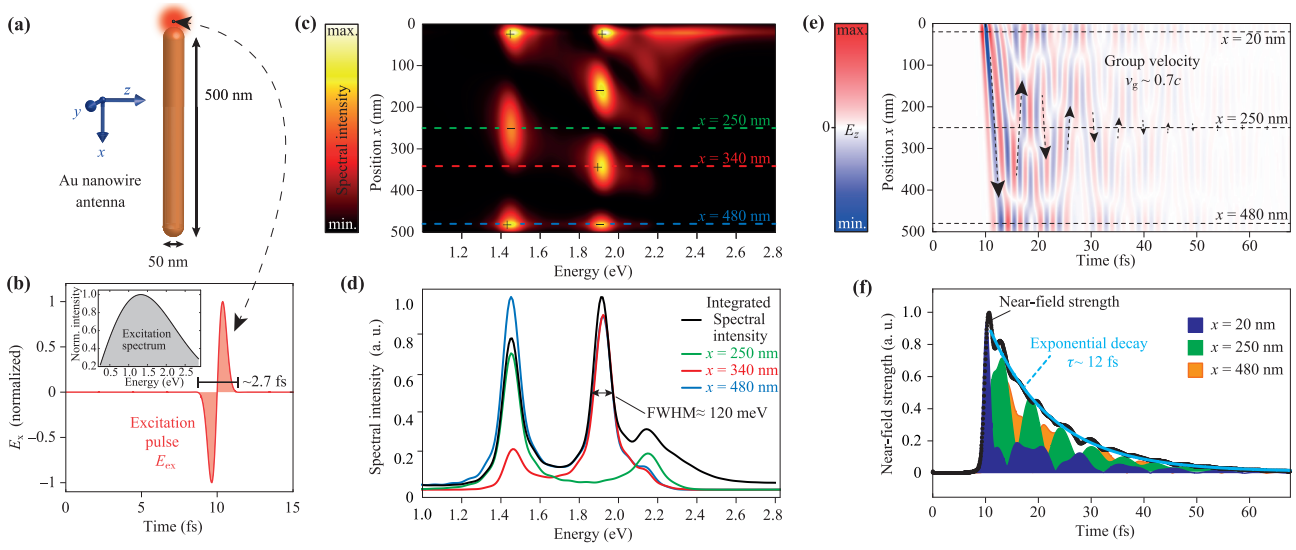

Fig. 1 FDTD simulation illustrating the relevant scales for plasmonics. **(a)** Sketch of the three-dimensional (3D) FDTD model geometry. The dielectric function for Au was taken from Johnson and Christy [12]. **(b)** Pulsed excitation field $E_{ex}//x$ at the position of the point dipole source (at $x = -10$ nm, $y = z = 0$; see panel a). The total duration of the single-cycle pulse is ~ 2.7 fs. The corresponding energy spectrum (inset) features a broad excitation bandwidth (1.9 eV, FWHM), peaking at 1.3 eV. **(c)** Spectral distribution of the induced plasmonic near-field intensity (Fourier components of the induced wave packet, $|E_z(\omega)|^2$) along a straight line 10 nm above the wire, parallel to the wire long axis ($x = 0 - 500$ nm, $y = 0$ nm, $z = 35$ nm). Signs indicate the relative phase of the intensity antinodes of the excited resonant eigenmodes. Horizontal dashed lines indicate selected positions along the wire (see panel d). **(d)** Induced plasmonic near-field spectral intensity versus energy (black curve), calculated as the integral over the Fourier components $|E_z(\omega)|^2$ along the straight line defined above. Representative of the resonances excited by the broadband pulse, it exhibits peaks with a FWHM of $\simeq$120 meV corresponding to eigenmode damping. Colored curves illustrate the spectral dependence of the induced near-field intensity at different positions x along the wire, which correspond to the colored horizontal lines in panel c. **(e)** Time dependence of the induced plasmonic near-field amplitude $E_z(t)$ along the straight line defined above. Arrows indicate the back-and-forth reflections of the plasmonic wavefront; their slope provides an estimate of the corresponding group velocity $v_g \simeq 2.1 \times 10^8$ m·s^{-1} $\sim 0.7c$, and their length corresponds to the relative near-field strength. Horizontal dashed lines indicate selected positions along the wire (see panel f). **(f)** Induced plasmonic near-field strength (black data points) versus time, calculated as the integral over the field envelope of $E_z(t)$ along the straight line. Representative of the relative electromagnetic energy in the near field, it exhibits an overall monoexponential temporal decay corresponding to Ohmic losses (fitted solid blue line, $E_z \propto \exp(\frac{-(t-t_0)}{\tau})$), with a time constant $\tau \sim 12$ fs. Filled shaded curves represent the time dependence of the E_z field envelopes at different positions x along the wire, which correspond to the dashed horizontal lines in panel e.

stead have been developed more recently, thus enabling time-resolved measurements as well. Compared to the use of electron excitation, the use of optical excitation provides better selectivity in driving specific plasmon modes through its additional degrees of freedom (photon energy, polarization, angular orbital momentum, and angle of incidence) on the one hand, whereas on the other hand, the symmetry-based selection rules involved leave other modes optically inaccessible. The first of these optical excitation methods that was implemented is based upon the photoemission of electrons from a laser-excited specimen (so-called photoelectrons). When the energy of the exciting photon is sufficiently high (i.e., it exceeds the work function of the material), a photoelectron can be directly ejected from the specimen, corresponding to linear photoemission [Fig. 2(c)]. Because plasmons are not directly involved in this process, this mechanism does not provide information on the plasmonic properties of the sample. Lower-energy incident photons, however, can excite (multiple) plasmonic modes in the sample through light absorption [Fig. 2(d)]. These plasmonic modes can subsequently couple with another incident photon or photoexcited plasmon to eject a photoelectron [Fig. 2(e)]. Such nonlinear photoemission *does* depend on the plasmonic properties of the sample, which can thus be investigated using photoemission electron microscopy (PEEM), as described in Section 2.3.

The second, and youngest, of the combined techniques also uses optical excitation, but instead uses subsequently incident fast electrons to probe the sample.

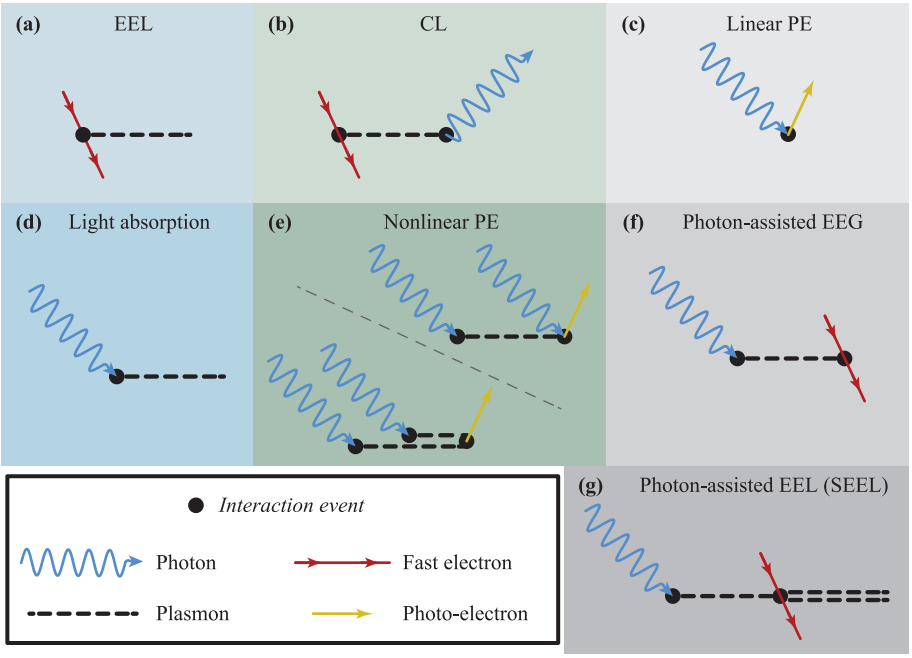

Fig. 2 Schematic diagrams of the elementary processes underlying the techniques discussed here. Reproduced, adapted, and expanded from Asenjo-Garcia and García de Abajo [13]. All schematics are drawn such that time flows from left to right. **(a)** In an EEL event, an incident fast electron excites a plasmon, losing energy in the process. **(b)** CL occurs when a plasmon excited through an EEL event decays radiatively by emitting a photon. **(c)** Linear photoemission corresponds to the direct ejection of a photoelectron (i.e., without plasmon excitation) upon photon absorption by the specimen. **(d)** At lower photon energies, incident photons are absorbed by the specimen, resulting in excitation of an optically active plasmonic mode. **(e)** In nonlinear photoemission, several incident photons excite one or several plasmons, leading to the ejection of one photoelectron. **(f)** In a photon-assisted EEG process, a photoexcited plasmon is absorbed by a subsequently incident fast electron. **(g)** Instead, in a photon-assisted, or stimulated EEL (SEEL) process, the subsequently incident fast electron emits a second plasmonic excitation.

When interacting with the sample, the fast electron can absorb the photoexcited plasmon [in a photon-assisted electron energy gain (EEG) process, Fig. 2(f)] or excite a second plasmon in the sample [through stimulated electron energy loss (SEEL), Fig. 2(g)]. Both types of photon-assisted events rely on the presence of the photoexcited plasmonic near field; thus, analysis of the transmitted electrons is particularly suitable for probing plasmonics. The corresponding photon-induced near-field electron microscopy (PINEM) methodology is discussed in Section 2.4.

In each section, we will provide an introductory overview of the technique that is reviewed. We first discuss the scientific emergence and underlying physical concepts of the method and then describe selected important and representative experiments that illustrate its current state of the art. Next, we consider the outlook for the technique and examine future directions it may take. In line with common usage in each field, we will interchangeably use the acronyms to refer to either the technique (where M stands for microscopy) and the apparatus (where M signifies microscope), as appropriate.

2.2 Electron Energy Loss Spectroscopy (EELS) & Cathodoluminescence (CL)

2.2.1 Spatially resolved EELS and CL experiments

The study of surface plasmons shares a long history with EELS and CL. Because the past few years have seen a number of excellent in-depth reviews [14–18], we restrict the introduction here to a brief historical and conceptual perspective of the field. The concept of surface plasmons was first introduced in 1957 by Ritchie, who calculated the corresponding energy loss of fast electrons when they passed through thin metal foils [19]. The predicted EELS resonance was subsequently measured in aluminum films by Powell and Swan as early as 1959 [20] and interpreted as a surface plasmon excitation by Stern and Ferrell in 1960 [21]. In parallel, in 1958, surface plasmons were predicted to also emit radiation [22], which was verified experimentally by recording CL spectra from silver films in 1960 [23]. EELS reports of surface plasmon maps, which visualize the spatial distributions of the excited plasmon modes, were first reported a couple of decades

later, perhaps most notably in Batson's observation of a coupled surface plasmon resonance in clusters of small metallic spheres in 1982 [24, 25]. Given the new and illustrative insights obtained by such spatially resolved experiments, many more EELS mapping studies on a variety of (nano-)objects followed [26–33]. In this period, however, energies in the visible (VIS) energy range and below ($E \lesssim 3$ eV) could not be accessed because of the limited experimental spectral resolution. It took a number of instrumental and analytical advances in terms of spectral and spatial resolution before, in 2001, Yamamoto *et al.* demonstrated the first CL-based mapping of different plasmon modes in the VIS range [Fig. 3(a)] [34]. This pioneering work then triggered experimental efforts to also extend EELS-based plasmon mapping to the sub-UV energy range. These efforts resulted in the first EELS maps in the near-infrared (NIR) and VIS range in 2007 [Fig. 3(b)] [35, 36].

In essence, both EELS and CL rely on the excitation of (surface) plasmons in the sample through interaction with the transient electric field generated by the fast electron beam. This transient electric field essentially corresponds to a very short excitation pulse, whose correspondingly broad frequency range effectively extends from (near) 0 to several tens or hundreds of electron volts, depending on the electron speed [14, 37–39]. Moreover, because this transient field has components both along and perpendicular to the electron propagation direction, the electron beam can couple to the photoexcitable plasmon modes, as well as to the plasmon modes that cannot be excited by light (for instance, multipolar modes in small quasistatic particles) [40]. Through this coupling to the electron's transient field, plasmonic EELS and CL signals scale with the electric field intensity of the corresponding plasmonic eigenmodes [41, 42]. Energy-selected images can then be used to map their spatial distribution [Figs. 3(a–c)]. The quantities measured are closely related to the projections of the electromagnetic local densities of states (EMLDOSs) [43] along the electron propagation direction, where the EELS signals measure the full EMLDOS [44, 45], and CL measures only the subset of these included in the radiative EMLDOS [46, 47].

In terms of instrumentation, the EELS and CL methodologies are complementary but conceptually similar. Typically, one focuses the electron beam in an electron microscope [either a scanning transmission electron microscope (STEM) or a scanning electron microscope (SEM)] down to a nanometer-scale diameter at the sample so that only a very local response is probed. In a microscope equipped with a CL detector, the light radiated by the electron-excited sample is collected by a parabolic mirror and subsequently analyzed by an optical spectrometer, yielding an optical spectrum resulting from the local interaction between the electron probe and the sample [Fig. 3(d)]. In EELS, one analyzes the spectral distribution of the transmitted electrons using an electron spectrometer instead, producing a local EEL spectrum [Fig. 3(e)]. In either case, one obtains a 3D dataset (x, y, E) containing a full energy spectrum for each x, y beam position by raster-scanning the beam laterally across the sample. In what is commonly referred to as spectrum imaging (SPIM) [48], one can then selectively analyze the spatial variation of the signal intensity in a given spectral range to spatially resolve the sample response at those energies. In practice, the resulting spatial resolution varies from a few nanometers to 10 nm, depending on the instrument, sample, and experimental conditions. Complementary information on the corresponding topography and morphology can be obtained simultaneously through either high-angle annular dark-field (HAADF) measurements or secondary electron detection, depending on the microscope.

An alternative EELS approach to plasmon mapping can be realized in a conventional transmission electron microscope (TEM) configuration, where instead of point-focusing, one employs a field-of-view electron beam to image the sample [Fig. 3(f)]. An example of this technique from Schaffer *et al.* [51] is depicted in Fig. 3(c). In this approach, the transmitted electron beam is analyzed by an advanced imaging energy filter [53, 54], which physically selects only electrons within a given spectral range and then reconstructs a two-dimensional (2D) filtered image corresponding to that energy range [55]. This technique is known as energy-filtered transmission electron microscopy (EFTEM) and is also used for time-resolved experiments, as discussed in Section 2.4. For a more in-depth comparison of EELS mapping in the SPIM and EFTEM configurations, we refer the reader to Ref. [56].

In contrast to that of EELS, the spectral resolution of the CL method does not depend on the energy distribution of the electron beam. Moreover, because the CL method detects the absolute photon energies, there is no zero energy peak in the spectrum that can potentially mask low-energy features [as opposed to the elastic zero loss peak (ZLP) in EELS; see the spectra in Figs. 3(d) and (f)]. For these reasons, the spectral resolution of the CL method has long been superior to that of EELS. On the other hand, the experimentally accessible energy range in EELS is generally much broader and more flexible.

2.2.2 EELS and CL plasmon mapping

Because the spatial and spectral properties of the plasmon modes are contained within the measured signals, EELS and CL are powerful tools to capture the physics behind these modes. As a simple example, plasmon dis-

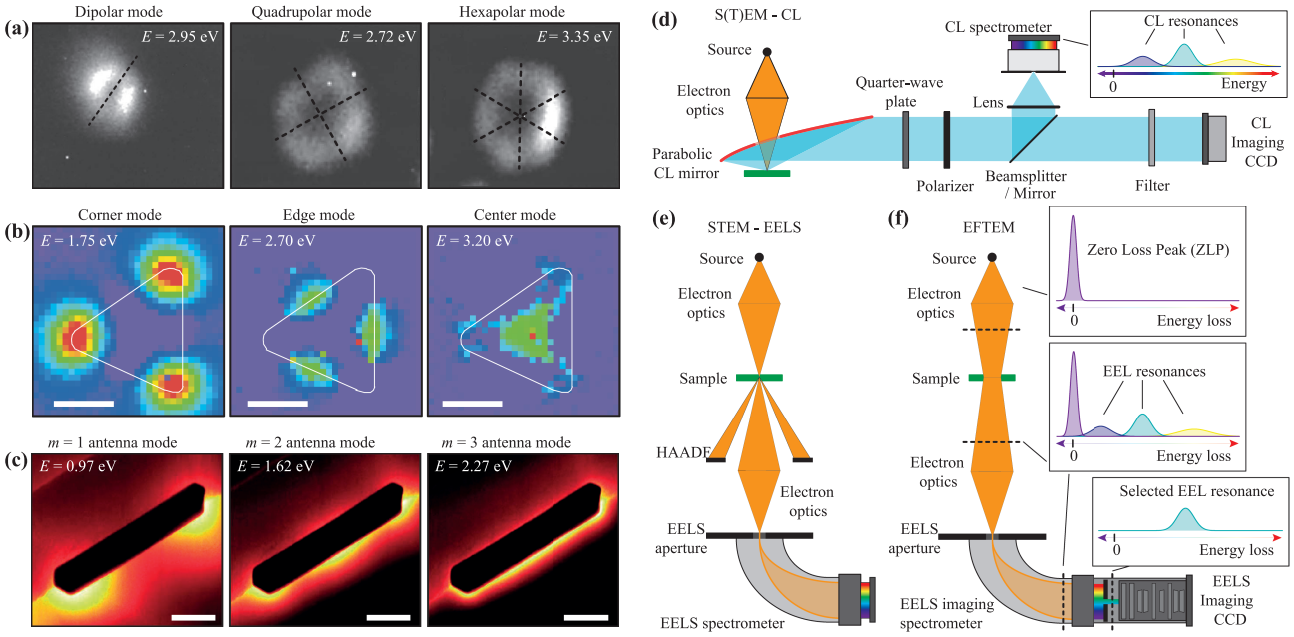

Fig. 3 Early surface plasmon mapping in the low-energy range (sub-3 eV). **(a)** CL spectral imaging of plasmon resonances in individual spherical Ag particles, where dipolar (left, particle diameter 140 nm), quadrupolar (middle, particle diameter 230 nm), and hexapolar modes (right, particle diameter 230 nm) are visualized. The CL emission is passed through a polarizer that lifts the degeneracy of the modes. Taken (with permission) and adapted from Yamamoto *et al.* [34]. **(b)** EELS spectral imaging of low-energy plasmon resonances in a silver triangular nanoprism (equilateral triangle, 78 nm sides), showing the corner (left), edge (middle), and center modes (right). Solid white line indicates the outer contour of the nanoprism, as deduced from the corresponding HAADF image. EELS spectra were processed using a maximum-likelihood deconvolution scheme [49]. Scale bars correspond to 30 nm. Taken (with permission) and adapted from Nelayah *et al.* [35]. **(c)** EFTEM mapping of low-energy Fabry–Pérot plasmon resonances in a Au nanorod antenna, where the $m = 1$ (left), $m = 2$ (middle), and $m = 3$ (right) antenna modes are identified (m indicates the mode order, which corresponds to the number of plasmonic field nodes along the antenna axis [50]). Scale bars correspond to 100 nm. Taken (with permission) and adapted from Schaffer *et al.* [51]. **(d)** Conceptual sketch of CL measurements, in part after Coenen *et al.* [52]. The nanometer-sized electron beam in an electron microscope (this can be a STEM or a SEM) is raster-scanned across the sample, while broadband CL radiation is collected using a parabolic mirror. In SPIM mode, the full CL spectrum is captured for each beam position using a spectrometer or tunable monochromator. Energy-selective maps are constructed from the 3D dataset in post-processing (see text). Advanced detection variants such as angle-resolved CL polarimetry use additional optical elements such as a quarter-wave plate, polarizer, and chromatic filter in combination with a 2D imaging CCD detector (see also Fig. 5 below). **(e)** Conceptual sketch of EELS measurements in the SPIM configuration [48]. The nanometer-sized electron beam in a STEM is raster-scanned across the sample, and the energy distribution of the transmitted electrons is recorded for each beam position using an EELS spectrometer. Here, energy-selective maps can also be constructed from the 3D dataset in post-processing. Complementary topographical and morphological information can be obtained by HAADF imaging. **(f)** Conceptual sketch of the alternative EFTEM approach, where the electron beam is spatially dispersed on the sample, and the transmitted electrons are energy-filtered by a post-column imaging filter to yield 2D selected energy images.

persion curves can be extracted from EELS and CL measurements to unveil the corresponding mode characters [see Fig. 4(a)]. This methodology was first applied by Vesseur *et al.*, who used CL to show that gold nanowires behave as one-dimensional (1D) plasmonic resonators [57]. The same approach was employed using EELS to demonstrate that the plasmon modes of flat nano-objects with arbitrary shapes have the same nature [55, 58, 59]. Subtle features of the modes, such as their spatial coherence, can also be probed [60]. Furthermore, because fast electrons and plane waves have different selection rules, EELS and CL can highlight plasmon modes that are not always accessible to all-optical techniques [Fig. 4(b)] [61–63].

Until recently, the main drawback of EELS was that its spectral resolution was limited to a few hundred millielectron volts because of the inherent energy spread of the incident electrons (the width of the ZLP). However, in recent years, the development of electron monochromators has pushed this energy spread down to around the 10 meV mark [68–70], resulting in two significant advances for EELS plasmon mapping. First, low-energy

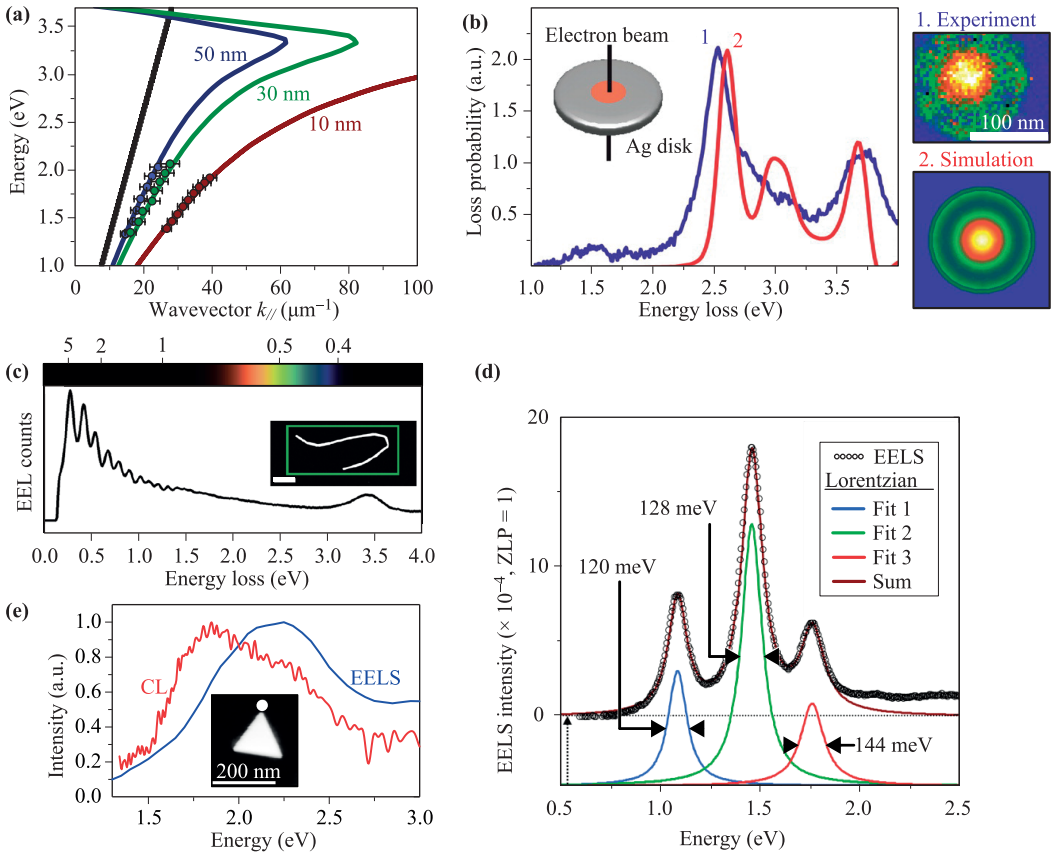

Fig. 4 Applications of EELS and CL plasmon mapping. **(a)** Dispersion relation of metal–insulator–metal (MIM) structures. The data points are obtained from CL measurements. The energies correspond to the CL resonances, and the wave vectors are obtained from the spatial distribution of the CL intensity. Solid lines show the dispersion relations of the plasmon modes of corresponding infinite interfaces as obtained from analytical calculations (for various insulator spacings). Black solid line is the light dispersion curve. The measurement agrees very well with the analytical calculations, showing that (i) the spatial and spectral properties of the modes can be derived from the measurement, and (ii) the MIM structures are plasmon resonators. Taken (with permission) and adapted from Kuttge *et al.* [64]. **(b)** EELS spectrum measured as an electron beam passed through the center of a silver nanodisk (solid blue line). The observed resonance is due to a breathing mode, whose spatial distribution is shown on the right. The experiments are in good agreement with numerical simulations (in red). The breathing mode escaped all previous optical measurements performed at normal incidence, as it can be photoexcited only under oblique angles of incidence [65]. Taken (with permission) and adapted from Schmidt *et al.* [63]. **(c)** EELS spectra averaged over a 2 μm long bent silver nanowire. Resonances as low as 0.17 eV are distinguished because the ZLP width is reduced by an electron monochromator. Taken (with permission) and adapted from Rossouw and Botton [66]. **(d)** EELS spectrum recorded close to a Au cross-shaped particle (data points). Single Lorentzian lineshapes (solid colored lines) were summed to fit the EELS spectrum. The observed peak broadening originating from the finite spectral resolution can be quantitatively taken into account in the fit because the incident electron energy spread is reduced by an electron monochromator. The numbers indicate the Lorentzian linewidths and correspond to the intrinsic mode damping values. Taken (with permission) and adapted from Bosman *et al.* [67]. **(e)** EELS (solid blue line) and CL (solid red line) spectra recorded at the tip of a single gold triangular nanoprism using a STEM (see inset). The CL resonance is shifted compared to the EELS resonance, showing that the dipolar plasmon mode resonates at different energies in EELS and CL. The shift occurs because EELS measures the energy lost by the fast electrons interacting with the particle, whereas CL measures the part of this energy radiated into the far field, and is related to the mode damping. Reproduced and adapted from Losquin *et al.* [42].

modes in the NIR-VIS range, which are particularly relevant for plasmonics [71, 72], have become accessible with the narrowing of the ZLP [Fig. 4(c)] [66, 73]. Second, the spectral widths of the resonances approach their intrinsic (physical) values, allowing the latter to be extracted quantitatively [Fig. 4(d)] [67]. Therefore, EELS now provides a nanometric probe of plasmonic mode damping that is entirely free of inhomogeneous broadening

[74, 75]. In contrast to that of EELS, the spectral resolution of CL does not suffer from the energy spread of the incoming electrons and can now reach 10 meV without any monochromator [76]. However, detection in the infrared is limited by the efficiency of optical spectrometers and detectors, and linewidth analysis is complicated by a broad luminescence background [14, 77]. On the other hand, an advantage of CL over EELS is that the light emission can be analyzed using optical elements, providing additional information about the modes (see next subsection).

Although EELS and CL plasmon mapping were first applied to simple nano-objects, they are being applied to increasingly complex samples, including particles a few nanometers in size [78, 79], objects with complex geometries [80, 81], manufactured nanoantennas [82, 83], metamaterials [84, 85], and disordered media [74, 86]. Over the last few years, EELS and CL have thus evolved toward accurate characterization techniques for plasmonic devices [64, 87], where EELS is used mainly for smaller, thinner objects, and CL is applied mostly to larger, thicker specimens. Moreover, the first combined EELS and CL experiment using a STEM demonstrated that the different behavior of EELS and CL leads to differences in the recorded EELS and CL signals of metallic nano-objects [Fig. 4(e)] [42]. Most notably, for small objects, only dipolar modes are probed by CL, whereas both dipolar and nondipolar modes can be probed using EELS. In the future, combined EELS and CL experiments should provide a powerful tool to quantify the radiative damping of plasmon modes [47, 88].

2.2.3 Advanced spectral imaging and tomography

As discussed in the previous sections, both EELS and CL are well-established methods for obtaining 2D maps of the electromagnetic eigenmodes of nanoscale objects and structures. In the most recent development, these fields have advanced into the realm of 3D mapping by applying electron beam tomography and 3D object reconstruction approaches [89–92]. In the latter, one records a series of planar signal maps (i.e., 2D projections) of a 3D object in various orientations, combining the orientational degrees of freedom of the sample with powerful post-processing techniques to allow for 3D image reconstruction. In 2013, 3D mapping of plasmon resonances through EELS tomography was both theoretically formulated by Horl *et al.* [94] and experimentally demonstrated by Nicoletti *et al.* [93] The latter used a combination of electron tomography, non-negative matrix factorization, [95] and compressed sensing [92, 96] to visualize the 3D spatial distribution of five distinct localized surface plasmon resonance (LSPR) components of a silver nanocube [Figs. 5(a) and (b)]. More recently, in 2015, Atre *et al.* [97] demonstrated the feasibility of 3D spectroscopic CL tomography by using a filtered back-projection approach [98–100] to reconstruct 3D CL intensity maps of a metal–dielectric nanocrescent at selected energies [Figs. 5(c) and (d)]. Although extremely valuable, these reconstructed 3D tomograms have been obtained under some rather restrictive assumptions and approximations (such as the use of a virtual or multi-object tilt series, an artificially imposed idealized object/substrate symmetry, application of the quasistatic approximation, and/or assumption of a single plasmon mode response), and the interpretation is nontrivial. Improvements on the tomography scheme will focus on extracting reliable quantitative information, for example, by applying inverse-problem schemes [101] or by using exact 3D nano-object geometries, which are themselves obtained through 3D electron tomography [102]. It has been established theoretically that a tomographic dataset can allow for reconstruction of the surface charge distribution of the plasmonic eigenmodes in the quasistatic approximation [94] or the full 3D EMLDOS in a general case [101]. In this regard, these methods are extremely promising. Successful retrieval of the surface charge distribution of plasmonic eigenmodes from an experimental dataset was reported recently [103]. Alternatively, a more conventional vector tomography approach could be implemented by decoupling the excitation and probing processes by combining optical plasmon excitation with EELS detection, as in electron energy gain spectroscopy (EEGS) [13, 104] and PINEM [105] (these are discussed in detail in Section 2.4 below).

Another recent advance in CL spectroscopy involves a different detection approach. Instead of spectrally analyzing all the CL radiation collected in a spectrometer, one can project the CL radiation onto a 2D CCD detector to capture the directionality of the CL emission [Fig. 5e]. In this scheme, each emission direction in the hemisphere above the sample is mapped onto a unique y, z position in the detection plane through a nontrivial coordinate transformation. In this way, one can extract the emission directionality of a plasmonic structure for any excitation position, as shown by Coenen *et al.* in 2011 [52]. Very recently, this approach was extended to additionally resolve polarization information, in what has been termed angle-resolved CL imaging polarimetry [106, 107]. In this case, one employs the polarization-sensitive detection method introduced by Yamamoto *et al.* [34] in 2001 by passing the collected CL radiation through a rotating plate polarimeter, and optionally a color (bandpass) filter, before detection [Fig. 5(e)]. By performing measurements at six polarimeter settings, one can thus fully characterize the polarization state of the angle-resolved CL emission in terms of Stokes parameters in the Mueller matrix formalism [108, 109]. One can then determine the relevant parameters of the CL radiation, such as the ra-

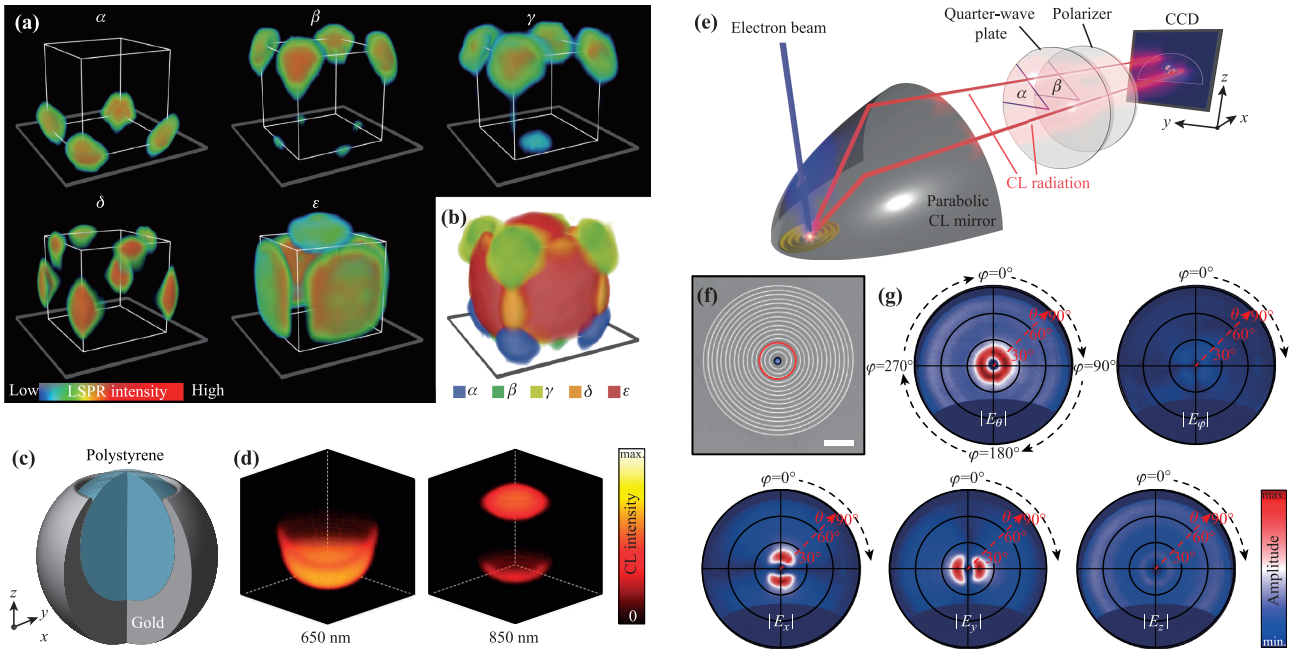

Fig. 5 Advanced SPIM experiments. **(a)** 3D EELS spectroscopic tomograms of the five hybridized localized surface plasmon resonance (LSPR) components of a silver nanocube on a Si_3N_4 substrate, described as a bottom-corner LSPR (α), a mixed top-corner and bottom-edge LSPR (β), a mixed top-corner and bottom-face LSPR (γ), a mixed top-edge and side-edge LSPR (δ), and a mixed top-face and side-face LSPR (ε). The plots, which correspond to voxel projections of tomographically reconstructed 3D datasets based on an experimental tilt series of 2D EELS maps, clearly visualize substrate-induced mode splitting in the nanocube. Color bar indicates the relative LSPR intensity. Taken (with permission) and adapted from Nicoletti *et al.* [93]. **(b)** Combined 3D rendering of the five plasmonic LSPR components of panel a, reflecting the overall symmetry of the nanocube. Taken (with permission) and adapted from Nicoletti *et al.* [93]. **(c)** Schematic of the metal–dielectric nanocrescent particle used in the first demonstration of CL spectroscopic tomography. Taken (with permission) and adapted from Atre *et al.* [97]. **(d)** 3D CL spectroscopic tomograms at two wavelengths reconstructed from an experimental tilt series of 2D CL maps of different nanocrescent particles in varying orientations (the tomograms thus represent an average object response). At higher energies (left panel), the detected signal originates from Au luminescence, which is concentrated primarily in the metallic shell of the particle. Conversely, at lower energy (right panel), the CL radiation is dominated by radiative decay of the crescent's plasmonic gap mode, near the tip. Taken (with permission) and adapted from Atre *et al.* [97]. **(e)** Scheme of CL polarimetry detection. As in conventional CL, a point-focused electron beam is used for local excitation. The radiation is collected using an in-column parabolic mirror and subsequently passed through a quarter-wave plate (oriented at an angle α), a linear polarizer (angle β), and an optional color filter (not shown) before being detected using a 2D CCD camera. The CCD image shown corresponds to the angle-resolved CL emission from a plasmonic bullseye structure (panel f) for $\alpha = \beta = 0°$. Taken (with permission) and adapted from Osorio *et al.* [107]. **(f)** SEM micrograph of a plasmonic bullseye nanostructure (pitch 600 nm). The blue circle indicates the position of the incident electron beam for the measurements shown here, and the scale bar corresponds to 2 μm. Taken (with permission) and adapted from Osorio *et al.* [107]. **(g)** Angle-resolved field amplitude distributions of the CL radiation emitted by the center-excited bullseye structure in panel f for spherical and Cartesian electric field components. These polar maps, which plot the CL emission intensity as a function of zenithal angle θ [ranging from 0° (surface normal) to 90°] and azimuthal angle ϕ (0°–360°), were retrieved from the experimentally measured polarimetry data after coordinate transformation and correction for solid angle sampling and parabolic mirror reflectivity. All components share the same relative color scale. Taken (with permission) and adapted from Osorio *et al.* [107].

tio of polarized to unpolarized light and the degrees of linear and circular polarization. This was experimentally demonstrated by Osorio *et al.* [107], who observed a radially polarized CL donut beam emitted from a symmetric plasmonic bullseye grating [Figs. 5(f) and (g)]. The ability to characterize both the directionality and polarization characteristics of CL emission is particularly interesting for asymmetrical excitation geometries and intrinsically asymmetric or chiral plasmonic nanostructures, such as Archimedean nanospirals [107, 110]. Moreover, for advanced plasmonic device development and functionality testing, angle-resolved CL imaging polarimetry offers a unique local probe that provides access to many important features such as emission handedness, opti-

cal activity, and material birefringence and anisotropy. Given the experimental feasibility of the corresponding detection upgrade and the wealth of information it can provide, angle-resolved CL imaging polarimetry can be expected to become a benchmark characterization technique in plasmonics in the near future.

Other current directions being explored include the use of electron vortex beams in EELS and time-resolved CL experiments. In the former, one utilizes either diffractive phase plates [111–114], magnetic lens aberrations [115], effective magnetic monopoles [116], or Kapitza–Dirac-type scattering from photons [117] to generate electron beams that carry angular orbital momentum (AOM). These so-called vortex electron beams can be used to measure magnetic phenomena on the nanoscale [118, 119] and enable magnetic plasmon mapping [120] and magnetic dichroism measurements in plasmonic structures [121]. Moreover, they allow for momentum-resolved AOM dichroism measurements in chiral plasmonic samples [122]. Most time-resolved CL studies to date have focused on semiconducting materials and nanostructures, as the attainable time-resolution is limited to hundreds of picoseconds (for interferometric temporal autocorrelation measurements [123]) or a few picoseconds (for streak camera measurements with pulsed electron sources [124, 125]). Pushing the resolution of time-resolved CL to the femtosecond regime, the time scale most relevant for plasmonics, is still a significant experimental challenge because conventional pump-probe schemes cannot be applied. Such schemes *are* feasible for time-resolved EELS measurements, however, which typically employ pulsed optical excitation combined with a pulsed electron probe [126]. As this approach offers femtosecond-scale time resolution, it is very suitable for measuring plasmon dynamics, as discussed in detail in Section 2.4 below.

2.3 Photoemission Electron Microscopy (PEEM)

2.3.1 Plasmon-mediated nonlinear PEEM

When light impinges on a solid, it can trigger the emission of photoelectrons from the material surface through the photoelectric effect. This well-known effect is the basis of PEEM. In PEEM, one images the spatial variation of the photoelectron emission (also called photoemission) from the surface of an illuminated sample. Images that reflect local differences in the overall photoemission intensity are then obtained by collecting all the emitted photoelectrons, regardless of their kinetic energy. Energy-filtered PEEM images, on the other hand, provide spectrally selective information and can be obtained using imaging energy filters, which filter out photoelectrons depending on their kinetic energies. In general, PEEM images depend strongly on the light source employed, as the photon energy dictates the photoemission mechanism. For instance, a UV lamp induces linear photoemission by providing photons whose energy is greater than the work function of the sample material [Fig. 2(c)]. In contrast, one can alternatively induce nonlinear photoemission using femtosecond laser pulses with sub-work-function photon energies [Fig. 2(e)].

Although nonlinear photoemission is in general relatively weak, it can be boosted through a surface plasmon resonance [133]. As an example, early PEEM experiments using a femtosecond laser on metallic samples reported strong localized nonlinear photoemission and attributed these hot spots to enhanced coupling through sample surface roughness [Fig. 6(a)] [127]. As proposed by Merschdorf *et al.* [128], a plasmon-enhanced photoemission mechanism can be rationalized from a semiclassical perspective [Fig. 6(b)]. In this picture, nonlinear photoemission occurs through coupling to the plasmonic near fields that are linearly induced by the femtosecond laser pulses incident on the sample [128]. A nonlinear PEEM image thus reflects the spatial variation of the photoinduced near field at its surface. This is in contrast to a complementary linear PEEM image obtained using a UV lamp, which instead reflects the sample morphology. This was demonstrated in 2005 by Cinchetti *et al.* [134], who proposed PEEM as a near-field technique.

Today, PEEM has become a well-established technique for imaging plasmonic near fields [see Fig. 6(c) for examples] and measuring the dispersion relations of surface plasmon polaritons (SPPs) [135, 136]. By keeping the laser fluences low to avoid space charge effects [137], one can achieve a spatial resolution of around 50 nm in conventional instruments. Aberration correctors can further push this resolution down to around 10 nm. We refer the interested reader to Ref. [138] for a general review of plasmonic near-field imaging using PEEM. In the following, we focus primarily on time-resolved PEEM experiments.

2.3.2 Time-resolved PEEM

The photon-in electron-out nature of PEEM makes it particularly suitable for time-resolved experiments. A generic time-resolved PEEM experiment for plasmonics is sketched in Fig. 7(a). Here, a sample is excited by two laser pulses that are delayed with respect to each other through an optical interferometer. The bandwidth of the first (pump) pulse overlaps the plasmon resonances of the sample. The pump pulse is thus resonantly scattered, generating a transient plasmonic near field at the sample. The delayed pulse can then serve as a direct or indirect probe of this induced transient field by modulating the photoemission at the sample. Scanning the delay between the two pulses allows one to obtain a series of images that contain information about the spatiotemporal evolution of the pump-induced plasmonic near field

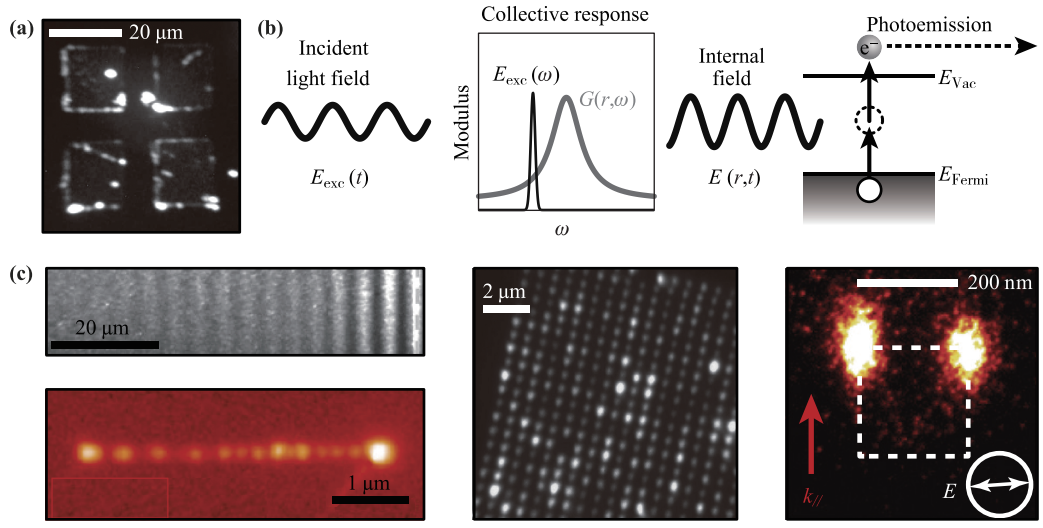

Fig. 6 Plasmon enhanced nonlinear photoemission. **(a)** Laser PEEM image showing strong localized nonlinear photoemission from a permalloy-covered silicon substrate. Taken (with permission) and adapted from Schmidt *et al* [127]. **(b)** Semiclassical picture of plasmon-enhanced photoemission. An excitation electric field $E_{\mathrm{exc}}(t)$ is elastically scattered and generates a spatially varying plasmonic near field $E(r,t)$ at the surface of the sample. In the frequency domain, the excitation spectrum $E_{\mathrm{exc}}(\omega)$ is multiplied by a classical scattering local response function $G(r,\omega)$ (here, a single harmonic response is assumed). The near field then drives nonlinear photoemission. Reproduced and adapted from Merschdorf *et al* [128]. **(c)** Examples of PEEM plasmonic near-field imaging: SPPs on metallic films [top left, taken (with permission) from Lemke *et al.* [129]] and nanowires [bottom left, taken (with permission) from Douillard *et al.* [130]], and LSPRs on nanoantenna arrays [middle, taken (with permission) from Wiemann *et al.* [131]] and single nano-objects [right, reproduced from Mårsell *et al.* [132]].

on the sample.

The most straightforward and widely used time-resolved PEEM experiment uses identical pump and probe pulses that are spatially overlapped on the sample. Schmidt *et al.* [143] first proposed such an experimental setup, in analogy to time-resolved two-photon photoemission experiments [144, 145]. In 2005, Kubo *et al.* employed this approach to identify and quantify different local resonances on a rough silver sample [Fig. 7(b)] [139]. In these experiments, the pump and probe pulses induce identical near fields at the sample surface, and the resulting near-field interference drives the nonlinear emission of electrons from the sample. Assuming that photoemission occurs via virtual states, the number of electrons emitted from a given point $\boldsymbol{r}$ on the sample surface as a function of the delay τ between the pump and probe pulses is described by a nonlinear autocorrelation of the pump-induced near field [140, 142]:

$$Y(\boldsymbol{r},\tau) \propto \int \mathrm{d}t\, |E_z(\boldsymbol{r},t) + E_z(\boldsymbol{r},t+\tau)|^{2n}\,, \qquad (1)$$

where E_z denotes a scalar projection of the linearly induced near field, and n is the nonlinearity order. This quantity can be compared to, for example, signals measured in optical nonlinear interferometric experiments [146, 147]. The obvious advantage of experiments such as these is that they are the simplest time-resolved PEEM experiments to perform. The drawback is that the measured signal is not a direct measurement of the spatiotemporal evolution of the near field, such that interpretation is not straightforward [129, 148, 149]. However, signal analysis can be supported by classical electrodynamics calculations, as was demonstrated for large metal surfaces [150], single nanoparticles [151, 152], or more complicated plasmonic devices [153, 154]. Such interferometric time-resolved experiments have recently been extended to few-light-cycle laser pulses, enabling the measurement of extremely short-lived transient near fields involving multiple plasmonic eigenmodes within single nanoparticles [Fig. 7(c)] [140]. Most generally, it is now well established that such experiments provide qualitative insight about the near-field temporal envelope and instantaneous oscillation frequency [140, 155].

Variants of the interferometric experiment described above use different pump and probe pulses with the same spectral bandwidth. Here, the measured photoemission signal can be viewed as a local nonlinear cross-correlation of the pump- and probe-induced near fields [142]. Such an experimental scheme can be useful for probing the pump-induced near field more directly. As an example, Gong *et al.* used spatially separated pump and probe beams to directly visualize SPP propagation

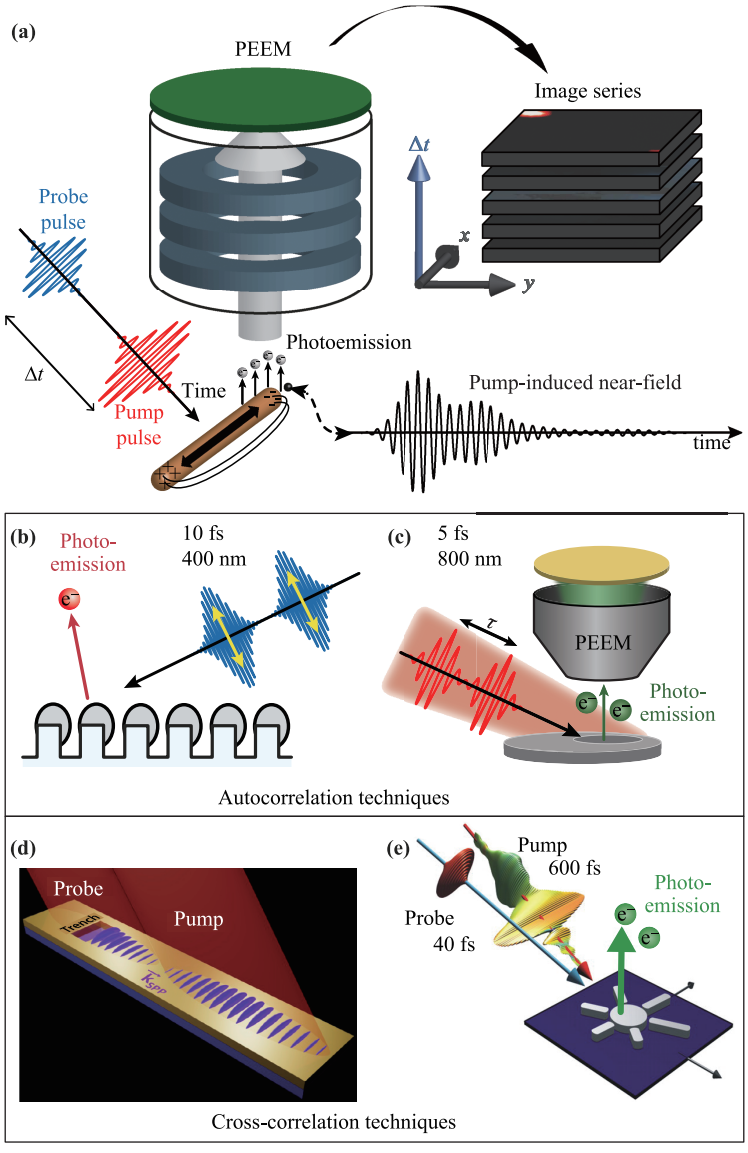

Fig. 7 **(a)** Sketch of a time-resolved PEEM experiment for plasmonics. Two laser pulses are incident on a sample in sequence. The delayed pulse probes the transient near field induced by the first pulse by modulating the photoemission at the sample. A series of images that contains information about the spatiotemporal evolution of the transient near field is obtained by scanning the delay Δt between the two pulses. Generally, two types of two-pulse techniques can be distinguished: those in which the pump and probe pulses are identical and overlap spatially (autocorrelation techniques) and those in which they differ (cross-correlation techniques). **(b)** 10 fs UV pulses induce photoemission from a rough silver sample by exciting various plasmon modes at different sites. Reproduced and adapted from Kubo *et al.* [139]. **(c)** 5 fs IR pulses induce photoemission from single ellipsoidal particles by exciting multiple longitudinal modes. Reproduced and adapted from Mårsell *et al.* [140]. **(d)** A probe pulse spatially separated from a pump pulse detects the near field of a pump-induced SPP propagating along a gold film. Taken (with permission) and adapted from Gong *et al.* [141]. **(e)** A short (40 fs) probe pulse samples the near field induced by a long (600 fs) pump pulse on a silver nanostructure. Taken (with permission) and adapted from Aeschlimann *et al.* [142].

on a metal surface [Fig. 7(d)] [141]. This experimental approach was recently extended to pump and probe pulses with different polarizations in normal incidence PEEM experiments, allowing for precise investigation of the physical mechanism underlying the image contrast [156, 157]. Furthermore, Aeschlimann *et al.* combined complex-shaped pump pulses with much shorter probe pulses (several hundreds of femtoseconds vs. 40 fs) [142]. In the latter case, the measured signal corresponds to the temporal envelope of the pump-induced near field

sampled with a temporal resolution given by the probe pulse duration [Fig. 7(e)].

2.3.3 *Toward attosecond-resolved direct near-field measurements*

In the previous subsection, we discussed a variety of time-resolved PEEM setups used to measure the spatiotemporal variation of plasmonic near fields. As should be clear from this discussion, the main advantage of time-resolved PEEM experiments is that both the pump and probe are optical, which offers great flexibility in experiments. Both the pump and probe can be manipulated using well-established pulse-shaping technology [159]. Arbitrarily complex experiments can thus be performed to measure the sample response to light excitation [160, 161]. Asymmetric pump-probe experiments can also be performed by using, for example, a nonlinear harmonic of the pump pulse as a probe pulse.

Ideally, a time-resolved PEEM experiment would provide a direct movie of the plasmonic near field at the sample surface. This would happen when electrons photoemitted from the probe pulse encounter a near field that is "frozen in time", which requires that the photoemission induced by the probe pulse should occur during a time much shorter than one oscillation period of the pump-induced near field. Therefore, such direct measurements cannot be achieved using only commercial laser systems, whose pulse duration comes up against the single light oscillation cycle limit (a few femtoseconds at optical frequencies) [162]. The pulse duration can, however, be decreased beyond the femtosecond limit by using higher-frequency radiation, which can be obtained through nonlinear harmonic generation. In particular, high harmonic generation from intense laser pulse trains can generate attosecond pulses with a bandwidth falling within the extreme ultraviolet (XUV) range [163], which have been used to measure laser pulses directly in time [164]. Stockman *et al.* proposed to use these attosecond pulses as a probe in PEEM experiments to achieve direct access to the near-field spatiotemporal dynamics (Fig. 8) [158]. In contrast to the experiments discussed previously, here an energy analyzer is used to track the pump-induced plasmonic field. Electrons that are linearly emitted by the attosecond probe pulse are accelerated by the pump-induced plasmonic near field. Under the assumption of instantaneous acceleration [158], the kinetic energy of the electrons would then correspond to a measure of the instantaneous local plasmonic electric potential. However, further theoretical works have argued that the interpretation of such datasets would be less straightforward [165]. Today, any time-resolved

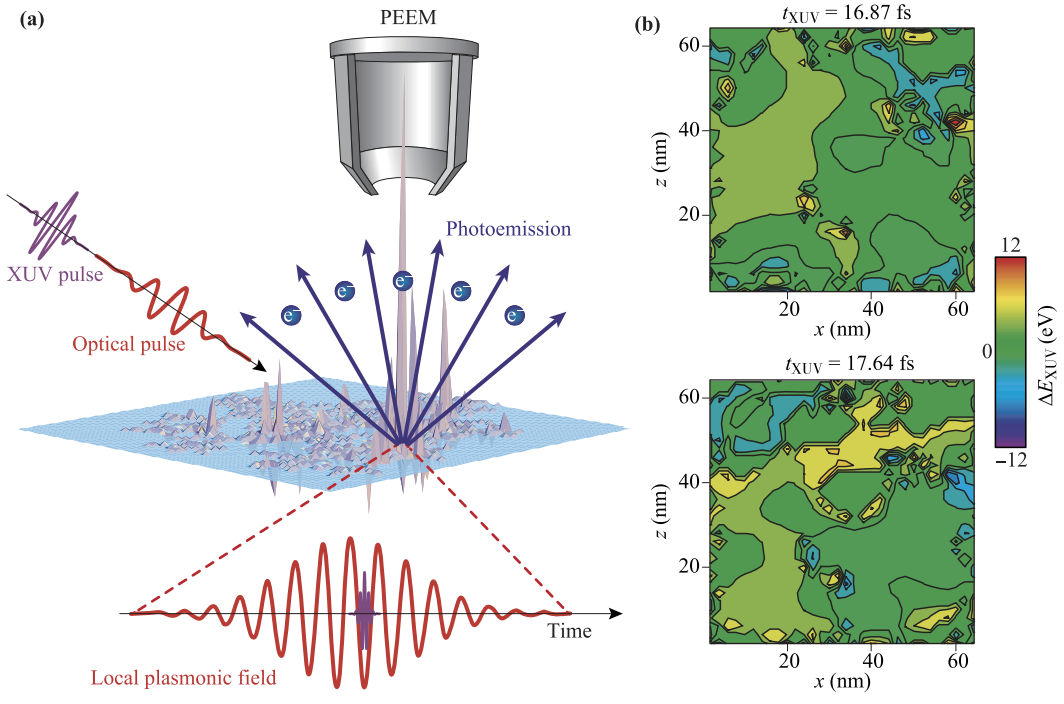

Fig. 8 Attosecond pump-probe PEEM experiment. **(a)** An XUV attosecond pulse induces linear emission of electrons that are accelerated by the near field generated by a femtosecond optical pulse. Taken (with permission) and adapted from Stockman *et al.* [158]. **(b)** Calculated energy distribution of electrons emitted locally from a random nanosystem for two incidence times of the attosecond pulse. The energy distribution of the electrons reflects the electric potential at the sample at each incidence time. Taken (with permission) and adapted from Stockman *et al.* [158].

PEEM experiment using attosecond pulses remains extremely challenging, although steps have been taken in this direction, and experimental effort is ongoing [166–170].

2.4 Photon-Induced Near-field Electron Microscopy (PINEM)

2.4.1 Electron energy gain (EEG)

The EELS technique discussed in Section 2.2 is based on processes in which fast probing electrons induce an excitation in a sample, thereby losing energy. The inverse energy exchange, in which fast electrons gain energy by interacting with the sample, can occur as well. Such processes were in fact observed as early as 50 years ago, when Boersch *et al.* recorded electrons gaining energies corresponding to thermally populated phonons when passing through a thin LiF film [171], as sketched in Fig. 9(a). As explained at the time, the intrinsic likelihood of either EEL or EEG occurring during the exchange is the same, so the overall probabilities of EEL and EEG are determined by the thermal occupation probability of the corresponding initial states [104]. Indeed, when the sample temperature was reduced, the thermal EEG originally observed in LiF was found to disappear [171]. Unfortunately, the consequence of this temperature dependence restricts these energy gains to energies on the order of $k_B T$, which corresponds to only $\simeq 26$ meV at room temperature (300 K).

This limitation is easily overcome, however, by photoexcitation of the sample and subsequent coupling to photoinduced nonequilibrium states, as originally suggested by Howie [172–175]. In this scenario, light of a particular excitation frequency ω induces an excitation in the sample (e.g., a plasmon), which is subsequently absorbed by the probe electron [Figs. 2(f) and 9(b)]. The energy gained thus corresponds exactly to the photon energy $E_{ph.} = \hbar\omega$, which can in principle be chosen to lie anywhere within the few-millielectron-volt to several-electron-volt range, depending on the source availability. It is important to note that such a net energy exchange cannot occur between freely copropagating electrons and photons in vacuum, as the photon momentum cannot match the necessary momentum change of the electron [104]. In contrast, spatially confined optical near fields, such as those corresponding to localized and propagating plasmonic modes, *do* carry the appropriate momentum to enable the exchange. Therefore, these photon-assisted electron energy transfers are entirely sample-mediated, which makes them ideally suited to application as selective and natural probes for plasmonics.

As is the case for energy loss features measured with EELS, the width of the energy-gain peak, which is located on the left ("negative energy loss") side of the ZLP in an EEL spectrum, is determined by the width of the ZLP (or, in some cases, by the electron analyzer). However, given the photon-assisted nature of the gain interaction, the entire gain peak necessarily corresponds to electrons that coupled to a material excitation having an energy within the bandwidth of the exciting illumination. Consequently, the integrated area of the electron gain peak is a measure of the sample response in this excitation bandwidth, as indicated in Fig. 9(c). It has thus been proposed that by varying the excitation energy (using well-established, limited-bandwidth tunable laser sources) and monitoring the integrated EEG response, one can perform EEGS, as sketched in the lower panel of Fig. 9(c). EEGS would combine the spatial resolution of electron microscopes with the potential submillielectron volt energy resolution of optical spectroscopy, but is yet to be realized experimentally [13, 14, 104, 172, 175]. Though EEGS would thus be able to substantially outperform current EELS technology in terms of spectral resolution, it would also encounter similar difficulties in resolving low-energy excitations (e.g., modes below 100 meV) because of (partial) masking of these features by the elastic ZLP tail and thermally assisted energy gain contributions.

Realization of EEGS faces several practical challenges. In addition to the need to excite a nanoscale object inside a TEM with a continuously tuned laser, the corresponding light intensity should also generate measurable probabilities of photon-assisted energy gain without damaging the sample. It is not surprising, then, that the first experimental observation of photon-assisted EEG in a TEM used temporally overlapping electron bunches and optical excitation pulses. Such a configuration can be achieved by generating electron bunches from a photocathode using UV laser pulses that are appropriately synchronized to the optical pump pulses. Using this methodology, also called PINEM, Barwick *et al.* photoexcited a transient evanescent near field on multiwalled carbon nanotubes and recorded its multiple energy transfers with the probing electrons in electron energy spectra [Fig. 9(d)] [105]. The observed equidistant gain and loss peaks correspond to different orders of photon-assisted net energy quantum exchange resulting from the complex evolution undergone by electrons during their subfemtosecond interaction time with the evanescent near field [178]. In such strongly driven near fields (i.e., in the presence of large numbers of a given evanescent mode), the probability of either plasmon absorption or emission by the electron is the same, so observed photon-assisted EEG (left of the ZLP) and SEEL events (right of the ZLP) occur symmetrically [13].

The true potential of PINEM becomes clear when one subsequently employs energy-filtered imaging [53, 54] to

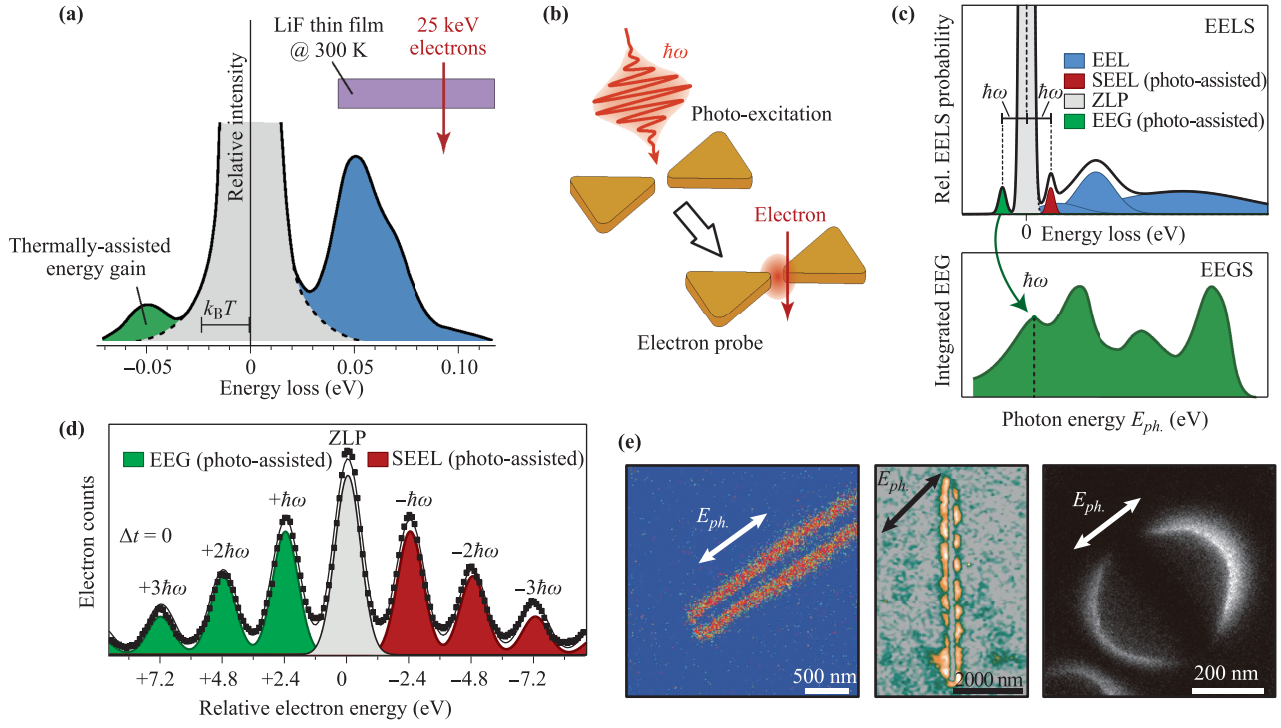

Fig. 9 Different contributions to energy exchange with fast electrons. **(a)** Early experimental evidence of EEG (shaded green area) through absorption of thermally populated phonons in a LiF thin film (sub-100 nm thickness) at room temperature. Reproduced from Boersch *et al.* [171] and adapted according to García de Abajo [14]. **(b)** Schematic mechanism of photoassisted contributions to electron energy exchange. A photon of energy $E_{ph.} = \hbar\omega$ photoinduces a localized (plasmonic) near field, which then interacts with a passing fast probe electron. Multiple energy exchange events can occur during the subfemtosecond interaction time. **(c)** EELS (upper panel) vs. EEGS (lower panel), after García de Abajo [14]. The upper panel shows a schematic EEL spectrum of a photoexcited sample ($E_{ph.} = \hbar\omega$). Color-coded peaks indicate the expected contributions to the EEL spectrum: Regular electron induced EEL contributions (bulk and surface plasmons, phonons, and so on), SEEL [stimulated loss (emission) of one $\hbar\omega$ quantum], the ZLP (here masking any thermally assisted EEG contributions), and photoassisted EEG [gain (absorption) of one $\hbar\omega$ quantum]. The integrated area under the EEG peak is proportional to the photoinduced near-field strength at frequency ω. A measurement of the integrated EEG signal as a function of the photon energy would provide a spectrum of the excitation modes of the sample, as sketched in the lower panel. **(d)** EEL spectrum of multiwalled carbon nanotubes photoexcited with an intense femtosecond pulse (at zero delay between optical and electron pulses, $\Delta t = 0$). The equidistant energy gain and loss peaks correspond to different orders of photon-assisted net energy quantum exchange. Color-coded shaded areas indicate the different spectral contributions. Taken (with permission) and adapted from Barwick *et al.* [105]. **(e)** Energy-filtered PINEM imaging of photoinduced evanescent near fields in various nanostructures: a multiwalled carbon nanotube [left, taken (with permission) and adapted from Barwick *et al.* [105]], a silver nanoantenna [middle, taken (with permission) and adapted from Piazza *et al.* [176]], and a protein vesicle [right, taken (with permission) and adapted from Flannigan *et al.* [177]]. All images were recorded using linearly polarized excitation light (polarization direction indicated by arrows marked $E_{ph.}$) at zero delay ($\Delta t = 0$).

select only the electrons that have gained energy. This yields a spatially resolved map of the photoinduced near field itself. Because photon-assisted contributions exist only on the electron gain side of the ZLP (at energies where the ZLP and thermal contributions are negligible), such PINEM images are thus ideally suited to provide background-free direct images of near-field distributions in plasmonic structures and devices. In their pioneering work, Barwick *et al.* [105] thus visualized the excited near field surrounding their carbon nanotubes. Since then, PINEM has been used for imaging in a multitude of different nanostructures, ranging from stained bacterial cells and protein vesicles [177] to metallic nanoparticles [179, 180] and nanoantennas [105, 176, 181] [Fig. 9(d)]. Time-resolved PINEM experiments can also be performed by varying the time delay between the optical excitation pulses and the UV laser pulses generating the electron bunches [182, 183]. In a very recent advance, Lummen *et al.* [183] directly visualized the interference of propagating SPPs in the first time-

resolved PINEM imaging experiments, enabling quantitative measurement of the corresponding propagation parameters (propagation speed, carrier wavelength, and decay length) even at buried metal–dielectric interfaces. The technique's flexibility is indicated by the fact that, in addition to imaging in a field-of-view approach, PINEM can also be performed using a nanoscopic scanning beam (in STEM fashion) [184, 185].

2.4.2 The electron–near-field interaction

In fact, such a nanoscale beam approach was recently used to experimentally confirm the nature of the interaction between the photoinduced near field and passing electrons [185]. Theoretically, the multiple energy transfers that occur during the subfemtosecond interaction time are well understood [13, 174, 178, 186]. Importantly, the electron couples only to the component of the evanescent near field along the electron propagation direction (i.e., perpendicular to the sample plane, often denoted E_z). During the interaction time, an electron can undergo N single-quantum exchange events (where N is the scattering order), so its net energy gain or loss corresponds to an integer number of photon quanta $|L| \leq N$ [13, 178]. Consequently, it is convenient to describe the final state of the electron as a superposition of equidistant quantum ladder states, as sketched in Fig. 10(a) [185]. In electron energy spectra, each of these energy levels is broadened by convolution with the much broader ZLP (typically, ZLP FWHMs are on the order of 1 eV in femtosecond-pulsed electron microscopes [181, 187]).

Figure 10(b) depicts the theoretical probability for the electron to end up in each of these channels as a function of the excitation light intensity [178]. Both semiclassical and quantum approaches yield the same expected behavior [13, 178, 185, 186], where the occupation prob-

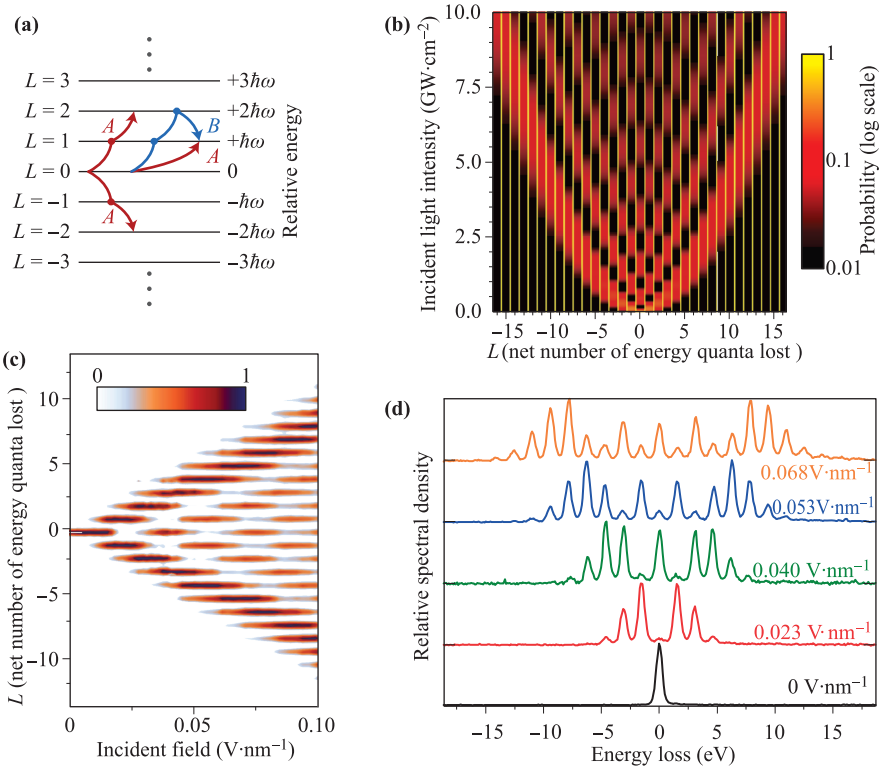

Fig. 10 Complex energy exchange between fast electrons and (plasmonic) near fields. **(a)** Diagram of coupled equidistant energy levels representing the possible electron energy states (experimentally observed in channels labeled L) during and after the subfemtosecond interaction time. Color-coded arrows indicate sequential (multi-)exchange pathways of type A (gain-only or loss-only) or B (both gain and loss processes). Reproduced and adapted from Feist *et al.* [185]. **(b)** Probability of photon-assisted energy gain (EEG, $L < 0$) and energy loss (SEEL, $L > 0$) for different net exchange channels L (see text) as a function of incident intensity. Taken (with permission) and adapted from García de Abajo *et al.* [178]. Energy spectra (horizontal cross sections) are normalized to their respective maxima. **(c)** Experimentally measured incident field strength dependence of the electron energy distribution after interaction with a uniform plasmonic near field. Taken (with permission) and adapted from Feist *et al.* [185]. **(d)** Experimental normalized electron energy spectra at selected incident field strengths of 0, 0.023, 0.040, 0.053, and 0.068 V·nm^{-1} (vertical cross sections in panel c). Taken (with permission) and adapted from Feist *et al.* [185].

ability for channel $|L|$ is well described by the L^{th}-order Bessel function of the first kind, $J_L(cE_{ex.})$ (here c is the near-field coupling constant describing the proportionality to the optical driving field $E_{\text{ex.}}$) [185]. Intuitively, this behavior can be understood by considering that the scattering order N increases with the incident field strength. Consequently, at lower fields (where N is limited), a given channel L is reachable exclusively by sequential gain-only or loss-only pathways [labeled A in Fig. 10(a)], and its occupation probability initially increases with $E_{\text{ex.}}$. At higher driving fields, contributions from more complex pathways become significant as well [i.e., those involving both gain and loss energy transfers, such as the pathway labeled B in Fig. 10(a)], and the ensuing interference between different quantum pathways results in the oscillatory behavior of the channel's occupation probability. In effect, the entire complex interaction can be viewed as a coherent phase and momentum modulation of the initial electron distribution by the optical driving field, in which the photoinduced plasmonic near field acts as a coherence-preserving intermediate coupler [13, 185].

To experimentally capture these phenomena, Feist *et al.* employed a variation of the PINEM technique in which the pulsed electron probe beam (≃800 fs pulse duration) was spatially narrowed to the nanoscale, and the exciting optical pulse was stretched to a 3.4 ps duration. In this way, the probing electrons encountered a mostly uniform and continuous near-field strength [185]. This is in contrast to ultrafast, field-of-view PINEM measurements (such as those described in Figs. 9 and 11), where probing electrons experience different field strengths due to the spatially and temporally varying near field, yielding energy spectra in which the channel occupation probability decreases monotonically with $|L|$. In their experiment, Feist *et al.* photoinduced a plasmonic near field on a sharp gold tip and measured the resulting energy distribution of the transmitted probe electrons as a function of the incident field strength [Figs. 10(c) and (d)]. The results essentially correspond to the observation of near-field-driven Rabi oscillations in the populations of equally spaced electron momentum states in the electron beam [188], in excellent agreement with established theory. On the whole, this experiment underlines the quantum coherent nature of the complex energy exchange processes between fast electrons and plasmonic near fields.

2.4.3 Hybrid imaging

As the previous sections made clear, all the details of the complex interaction with the plasmonic near field are encoded in the spatial and energy distributions of the transmitted electron beam [Fig. 11(a)]. Generally, when PINEM is applied in spectroscopy mode, the spatial distribution is collapsed (i.e., focused down), and the energy analyzer is set up to disperse the electrons according to their kinetic energy. This yields a 1D spectral distribution that reveals the quantized energy exchange of the interaction. In contrast, in PINEM imaging mode, the electron distribution is first energy-filtered by the analyzer (typically leaving only electrons that have gained energy), after which a 2D image of the original spatial distribution of these remaining electrons is projected onto the detector. This produces an image of the interferometric plasmonic field itself.

In a recent experiment, Piazza *et al.* [176] established a third, "hybrid" PINEM modality, in which the energy distribution of the electrons is projected along one dimension of the 2D detector, while one of the spatial axes of the electron distribution is projected along the other. As sketched in Fig. 11(b), this yields a hybrid energy–space map of the transmitted electron distribution, combining both spectroscopic and spatial information in the same image. By resonantly photoexciting a symmetric higher-order plasmonic mode in a silver nanowire antenna and aligning the latter with the spatial axis in such an energy–space map, they were able to simultaneously capture the dual aspects of the plasmonic near field. The experimental hybrid PINEM image in Fig. 11(c) visualizes both the spatial interference of the near field along the vertical direction (showing its wave-like nature) and its quantized energy exchange along the horizontal direction (indicating its particle-like character). These results, as well as the recently described diffraction of electron beams from plasmon waves [189], showcase the flexibility and richness that can be obtained by combining light and fast electrons to study plasmonic systems. Among similar lines, the possibility of interference between inelastic energy losses (EEL contributions) and photon-assisted losses (SEEL contributions) has recently been discussed as well [190].

3 Comparisons

The discussion of the different approaches in the previous sections shows that by employing a complementary ensemble of electron microscopy techniques, it is possible to probe the various characteristics of plasmonic systems in multiple dimensions of space, energy, and time. When electrons are used for probing, the main advantage over all-optical techniques, including (tip- or surface-enhanced) Raman microscopy and SNOM, is generally the superior spatial resolution, which can reach all the way to the atomic scale even in an ultrafast electron microscope [191]. Although all the techniques show similarities, one should bear in mind that the information obtained is not necessarily the same. As compared to that in conventional EELS and CL, the optical excita-

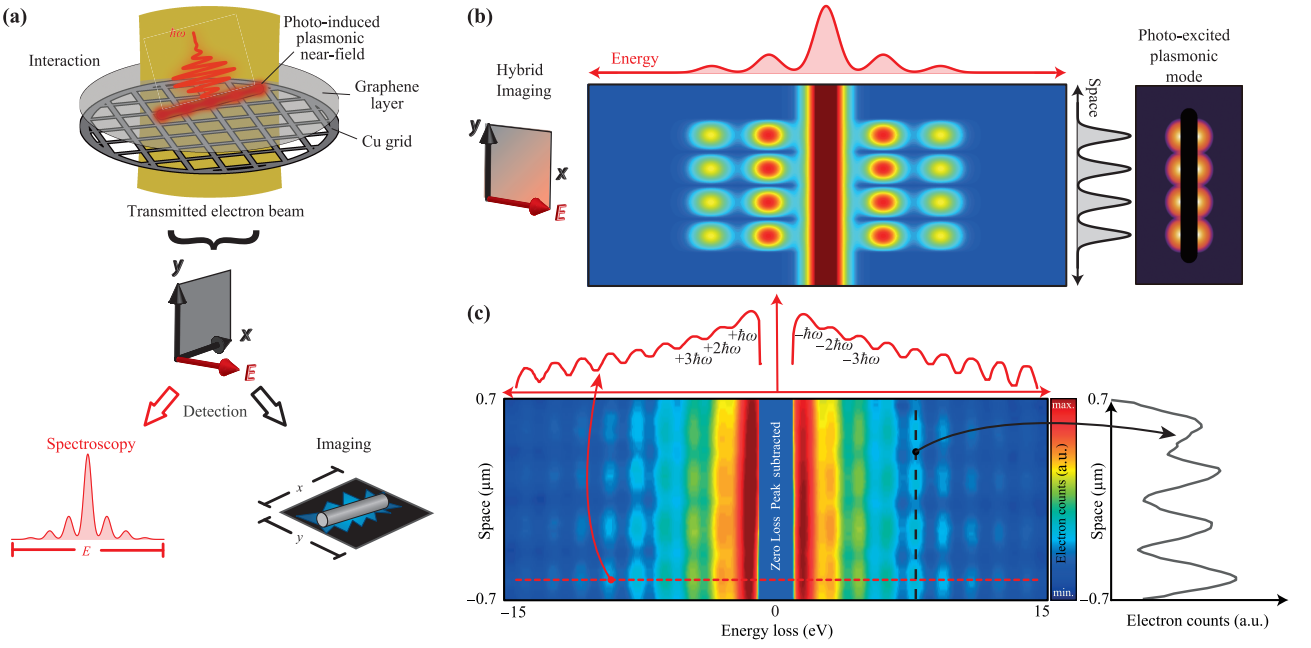

Fig. 11 Different PINEM methodologies. **(a)** Schematic of conventional PINEM approaches, which access either the spectral information (in spectroscopy mode) or the spatial information (in imaging mode) contained in the electron probe beam. **(b)** Concept of the hybrid PINEM approach, where the electron energy distribution is dispersed along the horizontal direction, and one spatial axis is projected onto the vertical direction. When this distribution is combined with a symmetric plasmonic mode that is photoinduced on an appropriately aligned nanoantenna (right), the resulting energy–space map of the transmitted electron beam exhibits both the spatial interference and energy quantization of the plasmonic near field. **(c)** Experimental realization of the hybrid energy–space imaging described in b. Horizontal and vertical traces correspond to cross sections of the energy–space map. In both the map and the traces, a Gaussian-fitted ZLP contribution was subtracted. Electron counts are plotted on a logarithmic scale. Taken (with permission) and adapted from Piazza *et al.* [176].

tion used in PEEM and PINEM allows for the possibility of varying the optical degrees of freedom such as the intensity, polarization, orbital momentum, and angle of incidence. This possibility offers the unique potential to separately excite and/or resolve degenerate photonic or plasmonic states. On the other hand, because of symmetry-based selection rules, using photons does restrict excitation to the subset of optically active plasmonic modes. To obtain information about all of the plasmonic eigenmodes, including the spatial distribution, resonance energy, and damping, EELS and CL are generally the established and preferred methods. Nonetheless, PEEM and PINEM can map evanescent near fields associated with light-excited plasmons as well (at the sample surface for PEEM and integrated along the electron trajectory for PINEM). Near-field images obtained using these techniques generally differ, as PINEM is usually performed with normal incidence excitation, whereas PEEM is most often performed with grazing incidence excitation [156]. Overall, PINEM offers better spatial resolution than PEEM and is typically incorporated into a more versatile TEM setup, which allows it to be easily combined with complementary microscopy techniques. On the other hand, PEEM setups are simpler, better established, and arguably lower maintenance. PINEM is not suitable for thick samples, whereas PEEM is not suitable for nonconducting samples.

To obtain spectral information about the sample, EELS and CL, as pure spectroscopy techniques, are by far the most natural and powerful methods. Access to spectroscopic information in PEEM and PINEM requires the use of a tunable laser source. Although this is possible [155, 192], both these techniques remain limited when resolving low-energy excitations. Decreasing the excitation energy in PEEM leads to lower signal intensities as the photoemission nonlinearity order increases, whereas PINEM in principle allows for an unrestricted choice of photon energy owing to its inherent decoupling of the plasmon excitation and probing processes. PINEM, however, faces the same issues at low energy as conventional EELS, being arguably more limited because of its pulsed sources. The latter offer fewer electrons and a somewhat inferior energy resolution (currently limited to $\simeq$0.6 eV [193]). To improve the energy resolution of PINEM, the challenge will be to combine pulsed sources with electron monochromator technology, keeping in mind an acceptable compromise in pulse duration and signal intensity. A perhaps more promising alternative is the EEGS tech-

nique discussed in Section 2.4.1. It was recently calculated that by using the strong near-field enhancement in resonant plasmonic structures, one could obtain measurable EEGS signals even under continuous-wave illumination at laser intensities as low as $\sim 10^8$ W·m^{-2} [13]. Considering this theoretical feasibility, in particular for plasmonics, and the recent experimental advances in PINEM microscopy [193], it is to be expected that EEGS and its potential submillielectron volt/subnanometer resolution will be experimentally realized in the near future. EEGS would then complement EELS and CL as a near-field spectroscopy technique.

In terms of measuring plasmon dynamics, CL poses significant practical limitations. Because CL signals correspond to spontaneous radiative decay, they are not readily triggered in a conventional pump-probe scheme. As a result, CL dynamics are limited by streak camera technology, which is currently limited to picosecond time scales. Time-resolved EELS measurements *are* possible in a pump-probe scheme, but they require separation of the excitation and probing processes. This could, in principle, be done using sequential pump and probe electron pulses, but in practice the number of electrons necessary for efficient plasmon excitation would drive the corresponding pulse duration out of the desired femtosecond range [194]. Instead, PEEM and PINEM, which use both electrons and photons, are well suited to time-resolved experiments and allow access to the near field in the time domain. Of the two techniques, PEEM offers more flexibility in terms of experimental degrees of freedom, as both pump and probe are optical. The time resolution of PEEM depends on the optical pulse durations and stability of the setup, and is currently close to its ultimate few-femtosecond single-cycle limit in the optical regime. In contrast, the time resolution of PINEM depends on the cross-correlation between the electron probe and the optical pump pulses. In practice, it is limited by the electron bunch duration at the sample, which exceeds the duration of the electron-generating UV pulses because of space charge effects and/or dispersion broadening during propagation in the microscope. The temporal resolution of time-resolved PINEM has recently been pushed down to the several-hundred-femtosecond mark [181, 187], enabling real-time observation of SPP propagation [183]. Moreover, by introducing a third optical pulse in a photon gating approach, Hassan *et al.* [182] were able to improve the time resolution of PINEM even further, to the point where it is limited by the optical pulse duration ($\simeq$200 fs in this case). Decreasing the electron pulse duration even further would be possible using advanced compression schemes [195]. These include microwave compression [196], which has recently been implemented in a femtosecond diffraction setup [197], and the use of standing optical waves to create so-called "temporal lenses" [198, 199]. Interestingly, the coherently modulated electron distribution discussed in Section 2.4.2 was simulated to evolve into an attosecond electron pulse train [185], which could allow for a new plasmonics-based route toward probing attosecond dynamics. On the PEEM side, the need to keep the excitation fluences at the sample low in order to avoid building up space charge has, to date, conflicted with the low repetition rate of attosecond pulse sources [166, 168]. In the near future, attosecond PEEM experiments should greatly benefit from the high-repetition-rate attosecond pulse sources enabled by state-of-the-art high-repetition-rate, high-intensity laser systems [169, 200].

4 Summary and general outlook

Overall, the rise of plasmonics research has brought together the electron microscopy, nanofabrication, spectroscopy, and ultrafast optical communities, resulting in an array of novel experimental approaches offering high spatial resolution combined with high spectral or temporal resolution. Well-established techniques such as EELS and CL have proven very valuable in spatially mapping surface plasmon modes. They are seeing continuous improvements in terms of resolution limits and quantitative analysis. Moreover, recent advanced implementations have opened the door to nanoscale 3D tomography and polarimetry of plasmonic systems, offering a wealth of new in-depth information. Hybrid techniques combining the use of photons and electrons, such as PEEM and PINEM, provide a unique window to map plasmonic near fields with nanometer spatial resolution on the femtosecond time scale and thus complement EELS and CL. Being younger, these methods still have ample room for advancement and specialization, with submillielectron volt and attosecond variants already being proposed. These techniques have distinctive strengths and specific purposes, and their complementarity and relative fields of applicability are starting to be explored through comparative experiments [42, 201–206]. Given the innovative ideas in the field and the versatility of electron microscopes, new approaches and modalities are bound to emerge, with the plasmonics community playing an important role as both driving force and beneficiary of these developments.

Acknowledgements A.L. acknowledges former and present colleagues for enjoyable discussions, most particularly Mathieu Kociak, Odile Stéphan, Erik Mårsell, Anne L'Huillier, and Anders Mikkelsen. A.L. was supported by NanoLund, the Swedish Research Council (VR), and the Knut and Alice Wallenberg Foundation. T.T.A.L. thanks Luca Piazza, Thomas LaGrange, Brett Barwick, Javier García de Abajo, and Fabrizio Carbone for fruitful

discussions and gratefully acknowledges financial support from the Research Executive Agency (REA) through Marie Curie IEF grant 623982.

References

1. W. L. Barnes, A. Dereux, and T. W. Ebbesen, Surface plasmon subwavelength optics, *Nature* 424(6950), 824 (2003)
2. E. Ozbay, Plasmonics: Merging photonics and electronics at nanoscale dimensions, *Science* 311(5758), 189 (2006)
3. L. Novotny and B. Hecht, Principles of Nano-Optics, Cambridge: Cambridge University Press, 2012, p. 564
4. M. S. Anderson, Locally enhanced Raman spectroscopy with an atomic force microscope, *Appl. Phys. Lett.* 76(21), 3130 (2000)
5. N. Hayazawa, Y. Inouye, Z. Sekkat, and S. Kawata, Metallized tip amplification of near-field Raman scattering, *Opt. Commun.* 183(1–4), 333 (2000)
6. P. L. Stiles, J. A. Dieringer, N. C. Shah, and R. P. V. Duyne, Surface-Enhanced Raman Spectroscopy, *Annu. Rev. Anal. Chem.* 1(1), 601 (2008)
7. M. D. Sonntag, E. A. Pozzi, N. Jiang, M. C. Hersam, and R. P. Van Duyne, Recent advances in tip-enhanced Raman spectroscopy, *J. Phys. Chem. Lett.* 5(18), 3125 (2014)
8. N. F. V. Hulst, N. P. de Boer, and B. Bölger, An evanescent-field optical microscope, *J. Microsc.* 163(2), 117 (1991)
9. H. Heinzelmann and D. W. Pohl, Scanning near-field optical microscopy, *Appl. Phys. A* 59(2), 89 (1994)
10. C. Bohm, J. Bangert, W. Mertin, and E. Kubalek, Time resolved near-field scanning optical microscopy, *J. Phys. D Appl. Phys.* 27(10), 2237 (1994)
11. H. Gersen, T. J. Karle, R. J. P. Engelen, W. Bogaerts, J. P. Korterik, N. F. van Hulst, T. F. Krauss, and L. Kuipers, Real-space observation of ultraslow light in photonic crystal waveguides, *Phys. Rev. Lett.* 94(7), 073903 (2005)
12. P. B. Johnson and R. W. Christy, Optical constants of the Noble metals, *Phys. Rev. B* 6(12), 4370 (1972)
13. A. Asenjo-Garcia and F. J. García de Abajo, Plasmon electron energy-gain spectroscopy, *New J. Phys.* 15(10), 103021 (2013)
14. F. J. García de Abajo, Optical excitations in electron microscopy, *Rev. Mod. Phys.* 82(1), 209 (2010)
15. E. J. R. Vesseur, J. Aizpurua, T. Coenen, A. Reyes-Coronado, P. E. Batson, and A. Polman, Plasmonic excitation and manipulation with an electron beam, *MRS Bull.* 37(08), 752 (2012)
16. M. Kociak and O. Stéphan, Mapping plasmons at the nanometer scale in an electron microscope, *Chem. Soc. Rev.* 43(11), 3865 (2014)
17. C. Colliex, M. Kociak, and O. Stéphan, Electron Energy Loss Spectroscopy imaging of surface plasmons at the nanometer scale, *Ultramicroscopy* 162, A1 (2016)
18. C. Cherqui, N. Thakkar, G. Li, J. P. Camden, and D. Masiello, Characterizing localized surface plasmons using electron energy-loss spectroscopy, arXiv: 1509.08430v2 (2015)
19. R. H. Ritchie, Plasma losses by fast electrons in thin films, *Phys. Rev.* 106(5), 874 (1957)
20. C. J. Powell and J. B. Swan, Origin of the characteristic electron energy losses in aluminum, *Phys. Rev.* 115(4), 869 (1959)
21. E. A. Stern and R. A. Ferrell, Surface plasma oscillations of a degenerate electron gas, *Phys. Rev.* 120(1), 130 (1960)
22. R. A. Ferrell, Predicted radiation of plasma oscillations in metal films, *Phys. Rev.* 111(5), 1214 (1958)
23. W. Steinmann, Experimental verification of radiation of plasma oscillations in thin silver films, *Phys. Rev. Lett.* 5(10), 470 (1960)
24. P. Batson, Surface plasmon coupling in clusters of small spheres, *Phys. Rev. Lett.* 49(13), 936 (1982)
25. P. Batson, A new surface plasmon resonance in clusters of small aluminum spheres, *Ultramicroscopy* 9(3), 277 (1982)
26. J. Cowley, Surface energies and surface structure of small crystals studied by use of a stem instrument, *Surf. Sci.* 114(2–3), 587 (1982)
27. L. Marks, Observation of the image force for fast electrons near an MgO surface, *Solid State Commun.* 43(10), 727 (1982)
28. M. Scheinfein, A. Muray, and M. Isaacson, Electron energy loss spectroscopy across a metal-insulator interface at sub-nanometer spatial resolution, *Ultramicroscopy* 16(2), 233 (1985)
29. A. Howie and R. Milne, Excitations at interfaces and small particles, *Ultramicroscopy* 18(1–4), 427 (1985)
30. M. Achèche, C. Colliex, H. Kohl, A. Nourtier, and P. Trebbia, Theoretical and experimental study of plasmon excitations in small metallic spheres, *Ultramicroscopy* 20(1–2), 99 (1986)
31. Z. Wang and J. Cowley, Size and shape dependence of the surface plasmon frequencies for supported metal particle systems, *Ultramicroscopy* 23(1), 97 (1987)
32. D. Ugarte, C. Colliex, and P. Trebbia, Surface- and interface-plasmon modes on small semiconducting spheres, *Phys. Rev. B* 45(8), 4332 (1992)
33. P. Moreau, N. Brun, C. A. Walsh, C. Colliex, and A. Howie, Relativistic effects in electron-energy-loss-spectroscopy observations of the Si/SiO_2 interface plasmon peak, *Phys. Rev. B* 56(11), 6774 (1997)
34. N. Yamamoto, K. Araya, and F. García de Abajo, Photon emission from silver particles induced by a high-energy electron beam, *Phys. Rev. B* 64(20), 205419 (2001)

35. J. Nelayah, M. Kociak, O. Stéphan, F. J. García de Abajo, M. Tencé, L. Henrard, D. Taverna, I. Pastoriza-Santos, L. M. Liz-Marzán, and C. Colliex, Mapping surface plasmons on a single metallic nanoparticle, *Nat. Phys.* 3(5), 348 (2007)
36. M. Bosman, V. J. Keast, M. Watanabe, A. I. Maaroof, and M. B. Cortie, Mapping surface plasmons at the nanometre scale with an electron beam, *Nanotechnology* 18(16), 165505 (2007)
37. J. T. van Wijngaarden, E. Verhagen, A. Polman, C. E. Ross, H. J. Lezec, and H. A. Atwater, Direct imaging of propagation and damping of near-resonance surface plasmon polaritons using cathodoluminescence spectroscopy, *Appl. Phys. Lett.* 88(22), 221111 (2006)
38. M. V. Bashevoy, F. Jonsson, A. V. Krasavin, N. I. Zheludev, Y. Chen, and M. I. Stockman, Generation of traveling surface plasmon waves by free-electron impact, *Nano Lett.* 6(6), 1113 (2006)
39. M. V. Bashevoy, F. Jonsson, K. F. Macdonald, Y. Chen, and N. I. Zheludev, Hyperspectral imaging of plasmonic nanostructures with nanoscale resolution, *Opt. Express* 15(18), 11313 (2007)
40. F. J. García de Abajo, Relativistic energy loss and induced photon emission in the interaction of a dielectric sphere with an external electron beam, *Phys. Rev. B* 59(4), 3095 (1999)
41. G. Boudarham and M. Kociak, Modal decompositions of the local electromagnetic density of states and spatially resolved electron energy loss probability in terms of geometric modes, *Phys. Rev. B* 85(24), 245447 (2012)
42. A. Losquin, L. F. Zagonel, V. Myroshnychenko, B. Rodríguez-González, M. Tencé, L. Scarabelli, J. Förstner, L. M. Liz-Marzán, F. J. García de Abajo, O. Stéphan, and M. Kociak, Unveiling nanometer scale extinction and scattering phenomena through combined electron energy loss spectroscopy and cathodoluminescence measurements, *Nano Lett.* 15(2), 1229 (2015)
43. R. Carminati, A. Cazé, D. Cao, F. Peragut, V. Krachmalnicoff, R. Pierrat, and Y. D. Wilde, Electromagnetic density of states in complex plasmonic systems, *Surf. Sci. Rep.* 70(1), 1 (2015)
44. F. J. García de Abajo and M. Kociak, Probing the photonic local density of states with electron energy loss spectroscopy, *Phys. Rev. Lett.* 100(10), 106804 (2008)
45. U. Hohenester, H. Ditlbacher, and J. R. Krenn, Electron-energy-loss spectra of plasmonic nanoparticles, *Phys. Rev. Lett.* 103(10), 106801 (2009)
46. M. Kuttge, E. J. R. Vesseur, A. F. Koenderink, H. J. Lezec, H. A. Atwater, F. J. García de Abajo, and A. Polman, Local density of states, spectrum, and far-field interference of surface plasmon polaritons probed by cathodoluminescence, *Phys. Rev. B* 79(11), 113405 (2009)
47. A. Losquin and M. Kociak, Link between cathodoluminescence and electron energy loss spectroscopy and the radiative and full electromagnetic local density of states, *ACS Photonics* 2(11), 1619 (2015)
48. C. Jeanguillaume and C. Colliex, Spectrum-image: The next step in EELS digital acquisition and processing, *Ultramicroscopy* 28(1–4), 252 (1989)
49. A. Gloter, A. Douiri, M. Tencé, and C. Colliex, Improving energy resolution of EELS spectra: An alternative to the monochromator solution, *Ultramicroscopy* 96(3–4), 385 (2003)
50. J. Dorfmüller, R. Vogelgesang, R. T. Weitz, C. Rockstuhl, C. Etrich, T. Pertsch, F. Lederer, and K. Kern, Fabry–Pérot resonances in one-dimensional plasmonic nanostructures, *Nano Lett.* 9(6), 2372 (2009)
51. B. Schaffer, U. Hohenester, A. Trügler, and F. Hofer, High-resolution surface plasmon imaging of gold nanoparticles by energy-filtered transmission electron microscopy, *Phys. Rev. B* 79(4), 041401 (2009)
52. T. Coenen, E. J. R. Vesseur, A. Polman, and A. F. Koenderink, Directional emission from plasmonic Yagi–Uda antennas probed by angle-resolved cathodoluminescence spectroscopy, *Nano Lett.* 11(9), 3779 (2011)
53. G. Kothleitner and F. Hofer, EELS performance measurements on a new high energy resolution imaging filter, *Micron* 34(3–5), 211 (2003)
54. A. Gubbens, M. Barfels, C. Trevor, R. Twesten, P. Mooney, P. Thomas, N. Menon, B. Kraus, C. Mao, and B. McGinn, The GIF Quantum, a next generation post-column imaging energy filter, *Ultramicroscopy* 110(8), 962 (2010)
55. L. Gu, W. Sigle, C. T. Koch, B. Ögüt, P. A. van Aken, N. Talebi, R. Vogelgesang, J. Mu, X. Wen, and J. Mao, Resonant wedge-plasmon modes in single-crystalline gold nanoplatelets, *Phys. Rev. B* 83(19), 195433 (2011)
56. M. Kociak, O. Stéphan, M. G. Walls, M. Tencé, and C. Colliex, Scanning transmission electron microscopy: Imaging and analysis, New York: Springer New York, 2011, Chap. Spatially Resolved EELS: The Spectrum-Imaging Technique and Its Applications, pp 163–205
57. E. J. R. Vesseur, R. de Waele, M. Kuttge, and A. Polman, Direct observation of plasmonic modes in au nanowires using high-resolution cathodoluminescence spectroscopy, *Nano Lett.* 7(9), 2843 (2007)
58. J. Nelayah, M. Kociak, O. Stéphan, N. Geuquet, L. Henrard, F. J. García de Abajo, I. Pastoriza-Santos, L. M. Liz-Marzán, and C. Colliex, Two-dimensional quasistatic stationary short range surface plasmons in flat nanoprisms, *Nano Lett.* 10(3), 902 (2010)
59. F. P. Schmidt, H. Ditlbacher, U. Hohenester, A. Hohenau, F. Hofer, and J. R. Krenn, Universal dispersion of surface plasmons in flat nanostructures, *Nat. Commun.* 5, 3604 (2014)
60. S. Mazzucco, N. Geuquet, J. Ye, O. Stéphan, W. Van Roy, P. Van Dorpe, L. Henrard, and M. Kociak, Ultralocal modification of surface plasmons properties in silver nanocubes, *Nano Lett.* 12(3), 1288 (2012)

61. M. W. Chu, V. Myroshnychenko, C. H. Chen, J. P. Deng, C. Y. Mou, and F. J. García de Abajo, Probing bright and dark surface-plasmon modes in individual and coupled noble metal nanoparticles using an electron beam, *Nano Lett.* 9(1), 399 (2009)
62. E. S. Barnard, T. Coenen, E. J. R. Vesseur, A. Polman, and M. L. Brongersma, Imaging the hidden modes of ultrathin plasmonic strip antennas by cathodoluminescence, *Nano Lett.* 11(10), 4265 (2011)
63. F. P. Schmidt, H. Ditlbacher, U. Hohenester, A. Hohenau, F. Hofer, and J. R. Krenn, Dark plasmonic breathing modes in silver nanodisks, *Nano Lett.* 12(11), 5780 (2012)
64. M. Kuttge, W. Cai, F. J. García de Abajo, and A. Polman, Dispersion of metal-insulator-metal plasmon polaritons probed by cathodoluminescence imaging spectroscopy, *Phys. Rev. B* 80(3), 033409 (2009)
65. M. K. Krug, M. Reisecker, A. Hohenau, H. Ditlbacher, A. Trügler, U. Hohenester, and J. R. Krenn, Probing plasmonic breathing modes optically, *Appl. Phys. Lett.* 105(17), 171103 (2014)
66. D. Rossouw and G. A. Botton, Plasmonic response of bent silver nanowires for nanophotonic subwavelength waveguiding, *Phys. Rev. Lett.* 110(6), 066801 (2013)
67. M. Bosman, E. Ye, S. F. Tan, C. A. Nijhuis, J. K. W. Yang, R. Marty, A. Mlayah, A. Arbouet, C. Girard, and M. Y. Han, Surface plasmon damping quantified with an electron nanoprobe, *Sci. Rep.* 3, 1312 (2013)
68. E. P. Bellido, D. Rossouw, and G. A. Botton, Toward 10 meV electron energy-loss spectroscopy resolution for plasmonics, *Microsc. Microanal.* 20(03), 767 (2014)
69. O. L. Krivanek, T. C. Lovejoy, M. F. Murfitt, G. Skone, P. E. Batson, and N. Dellby, Towards sub-10 meV energy resolution STEM-EELS, *J. Phys. Conf. Ser.* 522, 012023 (2014)
70. O. L. Krivanek, T. C. Lovejoy, N. Dellby, T. Aoki, R. W. Carpenter, P. Rez, E. Soignard, J. Zhu, P. E. Batson, M. J. Lagos, R. F. Egerton, and P. A. Crozier, Vibrational spectroscopy in the electron microscope, *Nature* 514(7521), 209 (2014)
71. A. N. Grigorenko, M. Polini, and K. S. Novoselov, Graphene plasmonics, *Nat. Photonics* 6(11), 749 (2012)
72. F. J. García de Abajo, Graphene plasmonics: Challenges and opportunities, *ACS Photonics* 1(3), 135 (2014)
73. D. Rossouw, M. Couillard, J. Vickery, E. Kumacheva, and G. A. Botton, Multipolar plasmonic resonances in silver nanowire antennas imaged with a subnanometer electron probe, *Nano Lett.* 11(4), 1499 (2011)
74. A. Losquin, S. Camelio, D. Rossouw, M. Besbes, F. Pailloux, D. Babonneau, G. A. Botton, J. J. Greffet, O. Stéphan, and M. Kociak, Experimental evidence of nanometer-scale confinement of plasmonic eigenmodes responsible for hot spots in random metallic films, *Phys. Rev. B* 88(11), 115427 (2013)
75. M. Bosman, L. Zhang, H. Duan, S. F. Tan, C. A. Nijhuis, C. W. Qiu, and J. K. Yang, Encapsulated annealing: enhancing the plasmon quality factor in lithographically-defined nanostructures, *Sci. Rep.* 4, 5537 (2014)
76. L. F. Zagonel, S. Mazzucco, M. Tencé, K. March, R. Bernard, B. Laslier, G. Jacopin, M. Tchernycheva, L. Rigutti, F. H. Julien, R. Songmuang, and M. Kociak, Nanometer scale spectral imaging of quantum emitters in nanowires and its correlation to their atomically resolved structure, *Nano Lett.* 11(2), 568 (2011)
77. B. J. M. Brenny, T. Coenen, and A. Polman, Quantifying coherent and incoherent cathodoluminescence in semiconductors and metals, *J. Appl. Phys.* 115(24), 244307 (2014)
78. J. A. Scholl, A. L. Koh, and J. A. Dionne, Quantum plasmon resonances of individual metallic nanoparticles, *Nature* 483(7390), 421 (2012)
79. S. Raza, S. Kadkhodazadeh, T. Christensen, M. Di Vece, M. Wubs, N. A. Mortensen, and N. Stenger, Multipole plasmons and their disappearance in few-nanometre silver nanoparticles, *Nat. Commun.* 6, 8788 (2015)
80. S. Mazzucco, O. Stéphan, C. Colliex, I. Pastoriza-Santos, L. Liz-Marzán, J. García de Abajo, and M. Kociak, Spatially resolved measurements of plasmonic eigenstates in complex-shaped, asymmetric nanoparticles: gold nanostars, *Eur. Phys. J.* 54(3), 33512 (2011)
81. A. Maity, A. Maiti, P. Das, D. Senapati, and T. K. Chini, Effect of intertip coupling on the plasmonic behavior of individual multitipped gold nanoflower, *ACS Photonics* 1(12), 1290 (2014)
82. H. Duan, A. I. Fernández-Domínguez, M. Bosman, S. A. Maier, and J. K. W. Yang, Nanoplasmonics: classical down to the nanometer scale, *Nano Lett.* 12(3), 1683 (2012)
83. T. Coenen, E. J. R. Vesseur, and A. Polman, Deep subwavelength spatial characterization of angular emission from single-crystal Au plasmonic ridge nanoantennas, *ACS Nano* 6(2), 1742 (2012)
84. F. von Cube, S. Irsen, R. Diehl, J. Niegemann, K. Busch, and S. Linden, From isolated metaatoms to photonic metamaterials: evolution of the plasmonic near-field, *Nano Lett.* 13(2), 703 (2013)
85. R. Verre, M. Svedendahl, N. Odebo Länk, Z. J. Yang, G. Zengin, T. J. Antosiewicz, and M. Käll, Directional light extinction and emission in a metasurface of tilted plasmonic nanopillars, *Nano Lett.* 16(1), 98 (2016)
86. M. Bosman, G. R. Anstis, V. J. Keast, J. D. Clarke, and M. B. Cortie, Light splitting in nanoporous gold and silver, *ACS Nano* 6(1), 319 (2012)
87. D. T. Schoen, A. C. Atre, A. García-Etxarri, J. A. Dionne, and M. L. Brongersma, Probing complex reflection coefficients in one-dimensional surface plasmon polariton waveguides and cavities using STEM EELS, *Nano Lett.* 15(1), 120 (2015)

88. J. Martin, M. Kociak, Z. Mahfoud, J. Proust, D. Gérard, and J. Plain, High-resolution imaging and spectroscopy of multipolar plasmonic resonances in aluminum nanoantennas, *Nano Lett.* 14(10), 5517 (2014)
89. R. A. Crowther, D. J. DeRosier, and A. Klug, The reconstruction of a three-dimensional structure from projections and its application to electron microscopy, *Proceedings of the Royal Society of London A: Mathematical, Physical and Engineering Sciences* 317, 319 (1970)
90. P. A. Midgley and R. E. Dunin-Borkowski, Electron tomography and holography in materials science, *Nat. Mater.* 8(4), 271 (2009)
91. D. A. De Winter, M. N. Lebbink, D. F. Wiggers De Vries, J. A. Post, and M. R. Drury, FIB-SEM cathodoluminescence tomography: Practical and theoretical considerations, *J. Microsc.* 243(3), 315 (2011)
92. R. Leary, Z. Saghi, P. A. Midgley, and D. J. Holland, Compressed sensing electron tomography, *Ultramicroscopy* 131, 70 (2013)
93. O. Nicoletti, F. de la Peña, R. K. Leary, D. J. Holland, C. Ducati, and P. A. Midgley, Three-dimensional imaging of localized surface plasmon resonances of metal nanoparticles, *Nature* 502(7469), 80 (2013)
94. A. Hörl, A. Trügler, and U. Hohenester, Tomography of particle plasmon fields from electron energy loss spectroscopy, *Phys. Rev. Lett.* 111, 076801 (2013)
95. D. D. Lee and H. S. Seung, Learning the parts of objects by non-negative matrix factorization, *Nature* 401(6755), 788 (1999)
96. E. J. Candes and M. B. Wakin, An introduction to compressive sampling, *IEEE Signal Process. Mag.* 25(2), 21 (2008)
97. A. C. Atre, B. J. M. Brenny, T. Coenen, A. García-Etxarri, A. Polman, and J. A. Dionne, Nanoscale optical tomography with cathodoluminescence spectroscopy, *Nat. Nanotechnol.* 10(5), 429 (2015)
98. I. Arslan, J. R. Tong, and P. A. Midgley, Reducing the missing wedge: High-resolution dual axis tomography of inorganic materials, *Ultramicroscopy* 106(11–12), 994 (2006)
99. M. Lyra and A. Ploussi, Filtering in SPECT image reconstruction, *Int. J. Biomed. Imaging* 2011, 693795 (2011)
100. X. Wang, R. Lockwood, M. Malac, H. Furukawa, P. Li, and A. Meldrum, Reconstruction and visualization of nanoparticle composites by transmission electron tomography, *Ultramicroscopy* 113, 96 (2012)
101. A. Hörl, A. Trügler, and U. Hohenester, Full three-dimensonal reconstruction of the dyadic green tensor from electron energy loss spectroscopy of plasmonic nanoparticles, *ACS Photonics* 2(10), 1429 (2015)
102. G. Haberfehlner, A. Trügler, F. P. Schmidt, A. Hörl, F. Hofer, U. Hohenester, and G. Kothleitner, Correlated 3D nanoscale mapping and simulation of coupled plasmonic nanoparticles, *Nano Lett.* 15(11), 7726 (2015)
103. S. M. Collins, E. Ringe, M. Duchamp, Z. Saghi, R. E. Dunin-Borkowski, and P. A. Midgley, Eigenmode tomography of surface charge oscillations of plasmonic nanoparticles by electron energy loss spectroscopy, *ACS Photonics* 2(11), 1628 (2015)
104. F. J. García de Abajo and M. Kociak, Electron energy-gain spectroscopy, *New J. Phys.* 10(7), 073035 (2008)
105. B. Barwick, D. J. Flannigan, and A. H. Zewail, Photon-induced near-field electron microscopy, *Nature* 462(7275), 902 (2009)
106. B. J. M. Brenny, D. van Dam, C. I. Osorio, J. Gómez Rivas, and A. Polman, Azimuthally polarized cathodoluminescence from InP nanowires, *Appl. Phys. Lett.* 107(20), 201110 (2015)
107. C. I. Osorio, T. Coenen, B. J. M. Brenny, A. Polman, and A. F. Koenderink, Angle-resolved cathodoluminescence imaging polarimetry, *ACS Photonics* 3(1), 147 (2016)
108. H. G. Berry, G. Gabrielse, and A. E. Livingston, Measurement of the Stokes parameters of light, *Appl. Opt.* 16(12), 3200 (1977)
109. C. Fallet, T. Novikova, M. Foldyna, S. Manhas, B. H. Ibrahim, A. D. Martino, C. Vannuffel, and C. Constancias, Overlay measurements by Mueller polarimetry in back focal plane, *MOEMS* 10(3), 033017 (2011)
110. G. Spektor, A. David, B. Gjonaj, G. Bartal, and M. Orenstein, Metafocusing by a Metaspiral Plasmonic Lens, *Nano Lett.* 15(9), 5739 (2015)
111. M. Uchida and A. Tonomura, Generation of electron beams carrying orbital angular momentum, *Nature* 464(7289), 737 (2010)
112. J. Verbeeck, H. Tian, and P. Schattschneider, Production and application of electron vortex beams, *Nature* 467(7313), 301 (2010)
113. B. J. McMorran, A. Agrawal, I. M. Anderson, A. A. Herzing, H. J. Lezec, J. J. McClelland, and J. Unguris, Electron vortex beams with high quanta of orbital angular momentum, *Science* 331(6014), 192 (2011)
114. K. Saitoh, Y. Hasegawa, K. Hirakawa, N. Tanaka, and M. Uchida, Measuring the orbital angular momentum of electron vortex beams using a forked grating, *Phys. Rev. Lett.* 111(7), 074801 (2013)
115. L. Clark, A. Béché, G. Guzzinati, A. Lubk, M. Mazilu, R. Van Boxem, and J. Verbeeck, Exploiting lens aberrations to create electron-vortex beams, *Phys. Rev. Lett.* 111(6), 064801 (2013)
116. A. Béché, R. Van Boxem, G. Van Tendeloo, and J. Verbeeck, Magnetic monopole field exposed by electrons, *Nat. Phys.* 10(1), 26 (2014)
117. J. Handali, P. Shakya, and B. Barwick, Creating electron vortex beams with light, *Opt. Express* 23(4), 5236 (2015)
118. J. Rusz and S. Bhowmick, Boundaries for efficient use of electron vortex beams to measure magnetic properties, *Phys. Rev. Lett.* 111(10), 105504 (2013)

119. P. Schattschneider, S. Löffler, M. Stöger-Pollach, and J. Verbeeck, Is magnetic chiral dichroism feasible with electron vortices? *Ultramicroscopy* 136, 81 (2014)

120. Z. Mohammadi, C. P. Van Vlack, S. Hughes, J. Bornemann, and R. Gordon, Vortex electron energy loss spectroscopy for near-field mapping of magnetic plasmons, *Opt. Express* 20(14), 15024 (2012)

121. X. Zambrana-Puyalto, X. Vidal, and G. Molina-Terriza, Angular momentum-induced circular dichroism in non-chiral nanostructures, *Nat. Commun.* 5, 4922 (2014)

122. A. Asenjo-Garcia and F. J. García de Abajo, Dichroism in the interaction between vortex electron beams, plasmons, and molecules, *Phys. Rev. Lett.* 113(6), 066102 (2014)

123. S. Meuret, L. H. G. Tizei, T. Cazimajou, R. Bourrellier, H. C. Chang, F. Treussart, and M. Kociak, Photon bunching in cathodoluminescence, *Phys. Rev. Lett.* 114(19), 197401 (2015)

124. M. Merano, S. Sonderegger, A. Crottini, S. Collin, P. Renucci, E. Pelucchi, A. Malko, M. H. Baier, E. Kapon, B. Deveaud, and J. D. Ganière, Probing carrier dynamics in nanostructures by picosecond cathodoluminescence, *Nature* 438(7067), 479 (2005)

125. T. Onuma, Y. Kagamitani, K. Hazu, T. Ishiguro, T. Fukuda, and S. F. Chichibu, Femtosecond-laser-driven photoelectron-gun for time-resolved cathodoluminescence measurement of GaN, *Rev. Sci. Instrum.* 83(4), 043905 (2012)

126. F. Carbone, O. H. Kwon, and A. H. Zewail, Dynamics of chemical bonding mapped by energy-resolved 4D electron microscopy, *Science* 325(5937), 181 (2009)

127. O. Schmidt, G. H. Fecher, Y. Hwu, and G. Schönhense, The spatial distribution of non-linear effects in multi-photon photoemission from metallic adsorbates on Si(111), *Surf. Sci.* 482–485, 687 (2001)

128. M. Merschdorf, C. Kennerknecht, and W. Pfeiffer, Collective and single-particle dynamics in time-resolved two-photon photoemission, *Phys. Rev. B* 70(19), 193401 (2004)

129. C. Lemke, T. Leißner, S. Jauernik, A. Klick, J. Fiutowski, J. Kjelstrup-Hansen, H. G. Rubahn, and M. Bauer, Mapping surface plasmon polariton propagation via counter-propagating light pulses, *Opt. Express* 20(12), 12877 (2012)

130. L. Douillard, F. Charra, Z. Korczak, R. Bachelot, S. Kostcheev, G. Lerondel, P. M. Adam, and P. Royer, Short range plasmon resonators probed by photoemission electron microscopy, *Nano Lett.* 8(3), 935 (2008)

131. C. Wiemann, D. Bayer, M. Rohmer, M. Aeschlimann, and M. Bauer, Local 2PPE-yield enhancement in a defined periodic silver nanodisk array, *Surf. Sci.* 601(20), 4714 (2007)

132. E. Mårsell, R. Svärd, M. Miranda, C. Guo, A. Harth, E. Lorek, J. Mauritsson, C. L. Arnold, H. Xu, A. L'Huillier, A. Mikkelsen, and A. Losquin, Direct subwavelength imaging and control of near-field localization in individual silver nanocubes, *Appl. Phys. Lett.* 107(20), 201111 (2015)

133. J. T. Stuckless and M. Moskovits, Enhanced two-photon photoemission from coldly deposited silver films, *Phys. Rev. B* 40(14), 9997 (1989)

134. M. Cinchetti, A. Gloskovskii, S. A. Nepjiko, G. Schönhense, H. Rochholz, and M. Kreiter, Photoemission electron microscopy as a tool for the investigation of optical near fields, *Phys. Rev. Lett.* 95(4), 047601 (2005)

135. T. Leißner, C. Lemke, J. Fiutowski, J. W. Radke, A. Klick, L. Tavares, J. Kjelstrup-Hansen, H. G. Rubahn, and M. Bauer, Morphological tuning of the plasmon dispersion relation in dielectric-loaded nanofiber waveguides, *Phys. Rev. Lett.* 111(4), 046802 (2013)

136. C. Lemke, T. Leißner, A. Klick, J. Fiutowski, J. W. Radke, M. Thomaschewski, J. Kjelstrup-Hansen, H. G. Rubahn, and M. Bauer, The complex dispersion relation of surface plasmon polaritons at gold/parahexaphenylene interfaces, *Appl. Phys. B* 116(3), 585 (2014)

137. N. M. Buckanie, J. Göhre, P. Zhou, D. von der Linde, M. Horn-von Hoegen, and F. J. Meyer Zu Heringdorf, Space charge effects in photoemission electron microscopy using amplified femtosecond laser pulses, *J. Phys.: Condens. Matter* 21(31), 314003 (2009)

138. L. Douillard and F. Charra, Photoemission electron microscopy, a tool for plasmonics, *J. Electron Spectrosc. Relat. Phenom.* 189(Suppl.), 24 (2013)

139. A. Kubo, K. Onda, H. Petek, Z. Sun, Y. S. Jung, and H. K. Kim, Femtosecond imaging of surface plasmon dynamics in a nanostructured silver film, *Nano Lett.* 5(6), 1123 (2005)

140. E. Mårsell, A. Losquin, R. Svärd, M. Miranda, C. Guo, A. Harth, E. Lorek, J. Mauritsson, C. L. Arnold, H. Xu, A. L'Huillier, and A. Mikkelsen, Nanoscale imaging of local few-femtosecond near-field dynamics within a single plasmonic nanoantenna, *Nano Lett.* 15(10), 6601 (2015)

141. Y. Gong, A. G. Joly, D. Hu, P. Z. El-Khoury, and W. P. Hess, Ultrafast imaging of surface plasmons propagating on a gold surface, *Nano Lett.* 15(5), 3472 (2015)

142. M. Aeschlimann, M. Bauer, D. Bayer, T. Brixner, S. Cunovic, F. Dimler, A. Fischer, W. Pfeiffer, M. Rohmer, C. Schneider, F. Steeb, C. Strüber, and D. V. Voronine, Spatiotemporal control of nanooptical excitations, *Proc. Natl. Acad. Sci. USA* 107(12), 5329 (2010)

143. O. Schmidt, M. Bauer, C. Wiemann, R. Porath, M. Scharte, O. Andreyev, G. Schönhense, and M. Aeschlimann, Time-resolved two photon photoemission electron microscopy, *Appl. Phys. B* 74(3), 223 (2002)

144. J. Lehmann, M. Merschdorf, W. Pfeiffer, A. Thon, S. Voll, and G. Gerber, Surface plasmon dynamics in silver nanoparticles studied by femtosecond time-resolved photoemission, *Phys. Rev. Lett.* 85(14), 2921 (2000)

145. M. Scharte, R. Porath, T. Ohms, M. Aeschlimann, J. Krenn, H. Ditlbacher, F. Aussenegg, and A. Liebsch, Do Mie plasmons have a longer lifetime on resonance than off resonance? *Appl. Phys. B* 73(4), 305 (2001)
146. B. Lamprecht, A. Leitner, and F. Aussenegg, SHG studies of plasmon dephasing in nanoparticles, *Appl. Phys. B* 68(3), 419 (1999)
147. B. Lamprecht, J. R. Krenn, A. Leitner, and F. R. Aussenegg, Resonant and off-resonant light-driven plasmons in metal nanoparticles studied by femtosecond-resolution third-harmonic generation, *Phys. Rev. Lett.* 83(21), 4421 (1999)
148. M. Bauer, C. Wiemann, J. Lange, D. Bayer, M. Rohmer, and M. Aeschlimann, Phase propagation of localized surface plasmons probed by time-resolved photoemission electron microscopy, *Appl. Phys. A* 88(3), 473 (2007)
149. F. J. M. zu Heringdorf, L. Chelaru, S. Möllenbeck, D. Thien, and M. H. von Hoegen, Femtosecond photoemission microscopy, *Surf. Sci.* 601, 4700 (2007)
150. A. Kubo, N. Pontius, and H. Petek, Femtosecond microscopy of surface plasmon polariton wave packet evolution at the silver/vacuum interface, *Nano Lett.* 7(2), 470 (2007)
151. Q. Sun, K. Ueno, H. Yu, A. Kubo, Y. Matsuo, and H. Misawa, Direct imaging of the near field and dynamics of surface plasmon resonance on gold nanostructures using photoemission electron microscopy, *Light Sci. Appl.* 2(12), e118 (2013)
152. E. Lorek, E. Mårsell, A. Losquin, M. Miranda, A. Harth, C. Guo, R. Svärd, C. L. Arnold, A. L'Huiller, A. Mikkelsen, and J. Mauritsson, Size and shape dependent few-cycle near-field dynamics of bowtie nanoantennas, *Opt. Express* 23(24), 31460 (2015)
153. C. Lemke, C. Schneider, T. Leißner, D. Bayer, J. W. Radke, A. Fischer, P. Melchior, A. B. Evlyukhin, B. N. Chichkov, C. Reinhardt, M. Bauer, and M. Aeschlimann, Spatiotemporal characterization of SPP pulse propagation in two-dimensional plasmonic focusing devices, *Nano Lett.* 13(3), 1053 (2013)
154. C. Lemke, T. Leissner, A. Evlyukhin, J. W. Radke, A. Klick, J. Fiutowski, J. Kjelstrup-Hansen, H. G. Rubahn, B. N. Chichkov, C. Reinhardt, and M. Bauer, The interplay between localized and propagating plasmonic excitations tracked in space and time, *Nano Lett.* 14(5), 2431 (2014)
155. Q. Sun, H. Yu, K. Ueno, A. Kubo, Y. Matsuo, and H. Misawa, Dissecting the few-femtosecond dephasing time of dipole and quadrupole modes in gold nanoparticles using polarized photoemission electron microscopy, *ACS Nano* 10(3), 3835 (2016)
156. P. Kahl, S. Wall, C. Witt, C. Schneider, D. Bayer, A. Fischer, P. Melchior, M. Horn-von Hoegen, M. Aeschlimann, and F. J. Meyer zu Heringdorf, Normal-incidence photoemission electron microscopy (NI-PEEM) for imaging surface plasmon polaritons, *Plasmonics* 9(6), 1401 (2014)
157. D. Podbiel, P. Kahl, and F. J. Meyer zu Heringdorf, Analysis of the contrast in normal-incidence surface plasmon photoemission microscopy in a pump–probe experiment with adjustable polarization, *Appl. Phys. B* 122(4), 1 (2016)
158. M. I. Stockman, M. F. Kling, U. Kleineberg, and F. Krausz, Attosecond nanoplasmonic-field microscope, *Nat. Photonics* 1(9), 539 (2007)
159. M. Aeschlimann, M. Bauer, D. Bayer, T. Brixner, F. J. García de Abajo, W. Pfeiffer, M. Rohmer, C. Spindler, and F. Steeb, Adaptive subwavelength control of nano-optical fields, *Nature* 446(7133), 301 (2007)
160. M. Aeschlimann, T. Brixner, A. Fischer, C. Kramer, P. Melchior, W. Pfeiffer, C. Schneider, C. Strüber, P. Tuchscherer, and D. V. Voronine, Coherent two-dimensional nanoscopy, *Science* 333(6050), 1723 (2011)
161. M. Aeschlimann, T. Brixner, D. Differt, U. Heinzmann, M. Hensen, C. Kramer, F. Lükermann, P. Melchior, W. Pfeiffer, M. Piecuch, C. Schneider, H. Stiebig, C. Strüber, and P. Thielen, Perfect absorption in nanotextured thin films via Anderson-localized photon modes, *Nat. Photonics* 9(10), 663 (2015)
162. T. Brabec and F. Krausz, Intense few-cycle laser fields: Frontiers of nonlinear optics, *Rev. Mod. Phys.* 72(2), 545 (2000)
163. P. Agostini and L. F. DiMauro, The physics of attosecond light pulses, *Rep. Prog. Phys.* 67(6), 813 (2004)
164. E. Goulielmakis, M. Uiberacker, R. Kienberger, A. Baltuska, V. Yakovlev, A. Scrinzi, T. Westerwalbesloh, U. Kleineberg, U. Heinzmann, M. Drescher, and F. Krausz, Direct measurement of light waves, *Science* 305(5688), 1267 (2004)
165. E. Skopalová, D. Y. Lei, T. Witting, C. Arrell, F. Frank, Y. Sonnefraud, S. A. Maier, J. W. G. Tisch, and J. P. Marangos, Numerical simulation of attosecond nanoplasmonic streaking, *New J. Phys.* 13(8), 083003 (2011)
166. A. Mikkelsen, J. Schwenke, T. Fordell, G. Luo, K. Klünder, E. Hilner, N. Anttu, A. A. Zakharov, E. Lundgren, J. Mauritsson, J. N. Andersen, H. Q. Xu, and A. L'Huillier, Photoemission electron microscopy using extreme ultraviolet attosecond pulse trains, *Rev. Sci. Instrum.* 80(12), 123703 (2009)
167. S. H. Chew, F. Süßmann, C. Späth, A. Wirth, J. Schmidt, S. Zherebtsov, A. Guggenmos, A. Oelsner, N. Weber, J. Kapaldo, A. Gliserin, M. I. Stockman, M. F. Kling, and U. Kleineberg, Time-of-flight-photoelectron emission microscopy on plasmonic structures using attosecond extreme ultraviolet pulses, *Appl. Phys. Lett.* 100(5), 051904 (2012)
168. E. Mårsell, C. L. Arnold, E. Lorek, D. Guenot, T. Fordell, M. Miranda, J. Mauritsson, H. Xu, A. L'Huillier, and A. Mikkelsen, Secondary electron imaging of nanostructures using extreme ultra-violet attosecond pulse trains and infra-red femtosecond pulses, *Ann. Phys.* 525(1–2), 162 (2013)

169. S. H. Chew, K. Pearce, C. Späth, A. Guggenmos, J. Schmidt, F. Süßmann, M. F. Kling, U. Kleineberg, E. Mårsell, C. L. Arnold, E. Lorek, P. Rudawski, C. Guo, M. Miranda, F. Ardana, J. Mauritsson, A. L'Huillier, and A. Mikkelsen, Imaging localized surface plasmons by femtosecond to attosecond time-resolved photoelectron emission microscopy - "ATTO-PEEM", in: Attosecond Nanophysics, Wiley-VCH Verlag GmbH and Co. KGaA, 2014, pp 325–364

170. B. Förg, J. Schötz, F. Süßmann, M. Förster, M. Krüger, B. Ahn, W. A. Okell, K. Wintersperger, S. Zherebtsov, A. Guggenmos, V. Pervak, A. Kessel, S. A. Trushin, A. M. Azzeer, M. I. Stockman, D. Kim, F. Krausz, P. Hommelhoff, and M. F. Kling, Attosecond nanoscale near-field sampling, *Nat. Commun.* 7, 11717 (2016)

171. H. Boersch, J. Geiger, and W. Stickel, Interaction of 25-keV electrons with lattice vibrations in LiF. Experimental evidence for surface modes of lattice vibration, *Phys. Rev. Lett.* 17(7), 379 (1966)

172. A. Howie, Electrons and photons: Exploiting the connection, *Inst. Phys. Conf. Ser.* 161, 311 (1999)

173. A. Howie, Photon-assisted electron energy loss spectroscopy and ultrafast imaging, *Microsc. Microanal.* 15(4), 314 (2009)

174. A. Howie, Photon interactions for electron microscopy applications, *Eur. Phys. J. Appl. Phys.* 54, 33502 (2011)

175. A. Howie, Stimulated excitation electron microscopy and spectroscopy, *Ultramicroscopy* 151, 116 (2015)

176. L. Piazza, T. T. Lummen, E. Quiñonez, Y. Murooka, B. W. Reed, B. Barwick, and F. Carbone, Simultaneous observation of the quantization and the interference pattern of a plasmonic near-field, *Nat. Commun.* 6, 6407 (2015)

177. D. J. Flannigan, B. Barwick, and A. H. Zewail, Biological imaging with 4D ultrafast electron microscopy, *Proc. Natl. Acad. Sci. USA* 107(22), 9933 (2010)

178. F. J. García de Abajo, A. Asenjo-Garcia, and M. Kociak, Multiphoton absorption and emission by interaction of swift electrons with evanescent light fields, *Nano Lett.* 10(5), 1859 (2010)

179. A. Yurtsever and A. H. Zewail, Direct visualization of near-fields in nanoplasmonics and nanophotonics, *Nano Lett.* 12(6), 3334 (2012)

180. A. Yurtsever, J. S. Baskin, and A. H. Zewail, Entangled nanoparticles: Discovery by visualization in 4D electron microscopy, *Nano Lett.* 12(9), 5027 (2012)

181. L. Piazza, D. J. Masiel, T. LaGrange, B. W. Reed, B. Barwick, and F. Carbone, Design and implementation of a fs-resolved transmission electron microscope based on thermionic gun technology, *Chem. Phys.* 423, 79 (2013)

182. M. T. Hassan, H. Liu, J. S. Baskin, and A. H. Zewail, Photon gating in four-dimensional ultrafast electron microscopy, *Proc. Natl. Acad. Sci. USA* 112(42), 12944 (2015)

183. T. T. A. Lummen, R. J. Lamb, G. Berruto, T. Lagrange, L. Dal Negro, F. J. García de Abajo, D. McGrouther, B. Barwick, and F. Carbone, Shaping, imaging and controlling plasmonic interference fields at buried interfaces, arXiv: 1604.01232 (2016)

184. A. Yurtsever, R. M. van der Veen, and A. H. Zewail, Subparticle ultrafast spectrum imaging in 4D electron microscopy, *Science* 335(6064), 59 (2012)

185. A. Feist, K. E. Echternkamp, J. Schauss, S. V. Yalunin, S. Schäfer, and C. Ropers, Quantum coherent optical phase modulation in an ultrafast transmission electron microscope, *Nature* 521(7551), 200 (2015)

186. S. T. Park, M. Lin, and A. H. Zewail, Photon-induced near-field electron microscopy (PINEM): Theoretical and experimental, *New J. Phys.* 12(12), 123028 (2010)

187. D. A. Plemmons, S. Tae Park, A. H. Zewail, and D. J. Flannigan, Characterization of fast photoelectron packets in weak and strong laser fields in ultrafast electron microscopy, *Ultramicroscopy* 146, 97 (2014)

188. B. Shore and J. Eberly, Analytic approximations in multi-level excitation theory, *Opt. Commun.* 24(1), 83 (1978)

189. F. J. García de Abajo, B. Barwick, and F. Carbone, Electron diffraction by plasmon waves, arXiv: 1603.07551 (2016)

190. N. Talebi, W. Sigle, R. Vogelgesang, and P. van Aken, Numerical simulations of interference effects in photon-assisted electron energy-loss spectroscopy, *New J. Phys.* 15(5), 053013 (2013)

191. H. S. Park, J. S. Baskin, O. H. Kwon, and A. H. Zewail, Atomic-scale imaging in real and energy space developed in ultrafast electron microscopy, *Nano Lett.* 7(9), 2545 (2007)

192. C. Hrelescu, T. K. Sau, A. L. Rogach, F. Jäckel, G. Laurent, L. Douillard, and F. Charra, Selective excitation of individual plasmonic hotspots at the tips of single gold nanostars, *Nano Lett.* 11(2), 402 (2011)

193. H. Liu, J. S. Baskin, and A. H. Zewail, Infrared PINEM developed by diffraction in 4D UEM, *Proc. Natl. Acad. Sci. USA* 113(8), 2041 (2016)

194. B. Barwick and A. H. Zewail, Photonics and plasmonics in 4D ultrafast electron microscopy, *ACS Photonics* 2(10), 1391 (2015)

195. A. Gliserin, M. Walbran, F. Krausz, and P. Baum, Sub-phonon-period compression of electron pulses for atomic diffraction, *Nat. Commun.* 6, 8723 (2015)

196. E. Fill, L. Veisz, A. Apolonski, and F. Krausz, Sub-fs electron pulses for ultrafast electron diffraction, *New J. Phys.* 8(11), 272 (2006)

197. G. F. Mancini, B. Mansart, S. Pagano, B. van der Geer, M. de Loos, and F. Carbone, Design and implementation of a flexible beamline for fs electron diffraction experiments, *Nucl. Instrum. Methods Phys. Res. Sect. A* 691, 113 (2012)

198. P. Baum and A. H. Zewail, Attosecond electron pulses for 4D diffraction and microscopy, *Proc. Natl. Acad. Sci. USA* 104(47), 18409 (2007)

199. S. A. Hilbert, C. Uiterwaal, B. Barwick, H. Batelaan, and A. H. Zewail, Temporal lenses for attosecond and femtosecond electron pulses, *Proc. Natl. Acad. Sci. USA* 106(26), 10558 (2009)

200. P. Rudawski, A. Harth, C. Guo, E. Lorek, M. Miranda, C. M. Heyl, E. W. Larsen, J. Ahrens, O. Prochnow, T. Binhammer, U. Morgner, J. Mauritsson, A. L' Huillier, and C. L. Arnold, Carrier-envelope phase dependent high-order harmonic generation with a high-repetition rate OPCPA-system, *Eur. Phys. J. D* 69, 70 (2015)

201. V. Myroshnychenko, J. Nelayah, G. Adamo, N. Geuquet, J. Rodríguez-Fernández, I. Pastoriza-Santos, K. F. MacDonald, L. Henrard, L. M. Liz-Marzán, N. I. Zheludev, M. Kociak, and F. J. García de Abajo, Plasmon spectroscopy and imaging of individual gold nanodecahedra: A combined optical microscopy, cathodoluminescence, and electron energy-loss spectroscopy study, *Nano Lett.* 12(8), 4172 (2012)

202. P. Melchior, D. Kilbane, E. J. Vesseur, A. Polman, and M. Aeschlimann, Photoelectron imaging of modal interference in plasmonic whispering gallery cavities, *Opt. Express* 23(25), 31619 (2015)

203. E. Ringe, C. J. DeSantis, S. M. Collins, M. Duchamp, R. E. Dunin-Borkowski, S. E. Skrabalak, and P. A. Midgley, Resonances of nanoparticles with poor plasmonic metal tips, *Sci. Rep.* 5, 17431 (2015)

204. M. Zhao, M. Bosman, M. Danesh, M. Zeng, P. Song, Y. Darma, A. Rusydi, H. Lin, C. W. Qiu, and K. P. Loh, Visible surface plasmon modes in single Bi_2Te_3 nanoplate, *Nano Lett.* 15(12), 8331 (2015)

205. J. A. Hachtel, C. Marvinney, A. Mouti, D. Mayo, R. Mu, S. J. Pennycook, A. R. Lupini, M. F. Chisholm, R. F. Haglund, and S. T. Pantelides, Probing plasmons in three dimensions by combining complementary spectroscopies in a scanning transmission electron microscope, *Nanotechnology* 27(15), 155202 (2016)

206. T. Coenen, D. T. Schoen, B. J. M. Brenny, A. Polman, and M. L. Brongersma, Combined electron energy-loss and cathodoluminescence spectroscopy on individual and composite plasmonic nanostructures, *Phys. Rev. B* 93(19), 195429 (2016)